

LEO- and RIS-Empowered User Tracking: A Riemannian Manifold Approach

Pinjun Zheng, *Graduate Student Member, IEEE*, Xing Liu, *Member, IEEE*,
and Tareq Y. Al-Naffouri, *Senior Member, IEEE*

Abstract—Low Earth orbit (LEO) satellites and reconfigurable intelligent surfaces (RISs) have recently drawn significant attention as two transformative technologies, and the synergy between them emerges as a promising paradigm for providing cross-environment communication and positioning services. This paper investigates an integrated terrestrial and non-terrestrial wireless network that leverages LEO satellites and RISs to achieve simultaneous tracking of the 3D position, 3D velocity, and 3D orientation of user equipment (UE). To address inherent challenges including nonlinear observation function, constrained UE state, and unknown observation statistics, we develop a Riemannian manifold-based unscented Kalman filter (UKF) method. This method propagates statistics over nonlinear functions using generated sigma points and maintains state constraints through projection onto the defined manifold space. Additionally, by employing Fisher information matrices (FIMs) of the sigma points, a belief assignment principle is proposed to approximate the unknown observation covariance matrix, thereby ensuring accurate measurement updates in the UKF procedure. Numerical results demonstrate a substantial enhancement in tracking accuracy facilitated by RIS integration, despite urban signal reception challenges from LEO satellites. In addition, extensive simulations underscore the superior performance of the proposed tracking method and FIM-based belief assignment over the adopted benchmarks. Furthermore, the robustness of the proposed UKF is verified across various uncertainty levels.

Index Terms—LEO satellite, reconfigurable intelligent surface, 9D tracking, Riemannian manifold, unscented Kalman filter.

I. INTRODUCTION

In the realm of modern wireless systems, the importance of advanced user tracking mechanisms is increasingly prominent. Current tracking methodologies encompass a wide range, including global navigation satellite systems (GNSS) [1], radio frequency identification (RFID) [2], advanced computer vision techniques [3], inertial navigation systems (INS) [4], acoustic sensors [5], laser [6], radar [7], and wireless sensor networks [8]. Among these technologies, using wireless radio signals stands out as a particularly innovative and effective solution [9]. The integration of tracking with wireless communication systems not only addresses the localization needs but also enhances the efficiency and reliability of communication networks [10]. Compared with other techniques, the high flexibility, expansive global reach, and inherent connectivity infrastructure of wireless communication systems make them well-suited for integration at different levels. In particular,

the transition from 5G to 6G heralds an era characterized by ultra-fast speeds, minimal latency, and exceptional reliability in wireless networks [11], [12]. This evolution significantly enhances the integration and adaptability of tracking systems across diverse domains, ranging from indoor scenarios to outdoor environments, and from ground-level applications to space-based contexts [13], [14].

In recent years, the resurgence of low Earth orbit (LEO) satellites, particularly in tandem with 5G and 6G networks, marks a significant evolution in the field [15], [16]. LEO satellites provide global coverage and reduced latency, key to enhancing communication and real-time tracking, navigation, and location-based services. Recent research has been actively investigating the potential of LEO communication satellites for opportunistic navigation as viable supplements or even alternatives to the traditional satellite-based localization systems, i.e., GNSS [17], [18]. This burgeoning interest is underpinned by a suite of distinctive advantages that LEO satellites offer over GNSS, including stronger signal power, vast constellations, and a broad spectrum of frequency diversity [19], [20]. In an era where precision, speed, and reliability are increasingly critical in both tracking and communication domains, the unique capabilities of LEO satellites present a compelling solution to meet these demands.

Similar to GNSS, LEO satellite signals inevitably undergo significant attenuation and disruption when navigating through urban and indoor environments, primarily due to obstacles like building structures, multipath interference, and overall reduced signal strength [21]. To tackle these challenges, integrating LEO satellites with the terrestrial network emerges as a promising solution. Reconfigurable intelligent surfaces (RISs) [22]–[24], as innovative devices capable of intelligently adapting and enhancing incoming electromagnetic waves, can be strategically deployed on the ground to enhance the reception of LEO satellite signals. Numerous literature has highlighted the substantial potential of RISs in enhancing the positioning capabilities of advanced wireless communication systems, e.g., [25]–[28]. Nowadays, initial research has shown that the collaborative design between LEO satellites and RISs can further extend the coverage and efficiency of LEO satellite signals [29], [30], thus boosting the positioning and tracking services [31]. The vast coverage of LEO constellations and the adaptive capabilities of RISs come together to form a more connected and monitored integrated wireless network, unlocking new potential for advanced tracking solutions.

While signals of LEO communication satellites and RISs potentially exhibit inherent compatibility [31], seamlessly in-

The authors are with the Electrical and Computer Engineering Program, Division of Computer, Electrical and Mathematical Sciences and Engineering (CEMSE), King Abdullah University of Science and Technology (KAUST), Thuwal, 23955-6900, Kingdom of Saudi Arabia.

tegrating these two systems into a cohesive unit still requires sophisticated signal processing techniques. This paper considers applying LEO satellites and RISs within wireless communication systems, a terrestrial and non-terrestrial integrated network, for comprehensive user tracking. Recognizing that traditional three-dimensional (3D) or six-dimensional (6D) tracking may fall short in contexts where grasping the full spectrum of motion dynamics is paramount, particularly in advanced contexts like automated vehicles and aircraft [32], this work employs nine-dimensional (9D) tracking to offer an exhaustive perspective. The 9D tracking encompasses the dynamical estimation of the user equipment (UE)'s 3D position, 3D velocity, and 3D orientation, simultaneously. Such a comprehensive approach is essential for the understanding and management of an object's movement, aligning with the intricate requirements of high-precision interaction, control, automation, and decision-making processes.

Addressing the 9D tracking problem in an integrated LEO satellites and RISs system is challenging due to the following reasons:

- *The observation function is nonlinear.* Typically, in a multiple-input multiple-output (MIMO) communication system, the observation for the UE state estimation is served by the geometric channel parameters obtained from the channel estimation process [10]. Such channel parameters can contain Doppler shifts, angle-of-arrivals (AoAs), angle-of-departures (AoDs), and channel delays. However, the mappings between these channel parameters and the unknown UE state are highly nonlinear, increasing the difficulty of the state estimation.
- *The unknown UE state is constrained.* While the UE position and velocity lie in Euclidean space, the UE orientation, usually characterized by a rotation matrix,¹ is constrained in the Lie group $SO(3)$ [34]. Such a non-Euclidean topological structure poses significant challenges for conventional tracking algorithms based on Euclidean space. Hence, advanced signal processing techniques are required to deal with this hybrid constraint in the joint 9D state estimation.
- *The statistics of the observation are unknown and time-varying.* Usually, the statistics of the observation are essential in designing estimation algorithms. Since the observation (i.e., geometric channel parameters) is obtained from channel estimation, the uncertainty in these estimated channel parameters depends on both the geometric configuration of the system and the performance of the adopted channel estimation algorithm. Even if we assume an efficient channel estimator is available, the estimation uncertainty still relies on the true UE state, which is unknown and time-varying. Therefore, how to approximate this uncertainty and assign an appropriate belief to the observation remains a critical issue.

¹The orientation can also be represented by, e.g., Euler angles, which is a parametrization of minimal dimension without constraints. However, such a parametrization would result in the so-called singularity problem, which can significantly degrade the estimation performance in certain areas of the state space [33]. For this reason, we choose to use the rotation matrix representation in this work.

Aiming to resolve the aforementioned problems, this paper proposes a novel Riemannian manifold-based unscented Kalman filter (UKF) method for the 9D user tracking in a hybrid LEO satellite-RIS system. The main contributions of this work can be summarized as follows:

- We define an advanced 9D user tracking system incorporating LEO satellites and RISs. A cooperative downlink signal transmission framework is proposed to coordinate different satellites and collect geometric channel parameters effectively. By exploring the acquired channel parameters and the UE's motion dynamics, this system offers a comprehensive tracking solution, allowing simultaneous determination of the 3D position, 3D velocity, and 3D orientation of the UE.
- To address the defined 9D tracking problem, we develop a constrained UKF algorithm on the Riemannian manifold. Specifically, the proposed algorithm addresses the key issues in the considered 9D tracking problem as follows.
 - By generating and propagating the sigma points, the employed UKF enables the approximation of the first and second-order moments of the unknown state following nonlinear functions through sample mean and variance calculations.
 - By applying the Riemannian manifold theory within the UKF framework, the estimation steps are streamlined within a curvature of high-dimensional space, which ensures that the tracking solutions naturally meet the desired constraints.
 - By computing the weighted mean of the Fisher information matrices over the generated sigma points, the uncertainty in the observation can be well approximated. Hence, an appropriate belief assignment principle is proposed, guaranteeing the accuracy of the measurement update steps in the UKF.
- Extensive simulations are conducted to evaluate the proposed system and algorithm.
 - The system is evaluated in a complex simulation environment, where the UE's trajectory goes through the rural, suburban, and urban scenarios with different scattering strengths and line-of-sight (LoS) probabilities. The results indicate that the integration of RISs can significantly enhance the tracking performance and mitigate the performance degradation in urban regions, particularly for the UE position estimation. Apart from that, simulation reveals a trade-off between the transmission overhead and the tracking performance. Moreover, the impact of different system parameters is widely tested, providing insights into the deployment of such collaborative tracking systems.
 - The performance of the proposed tracking algorithm is thoroughly validated. The proposed belief assignment principle demonstrates a significant performance enhancement over identical belief, rivaling the effectiveness of employing the true covariance matrix of observations in certain regions. Benchmarked against the classical unconstrained UKF, we

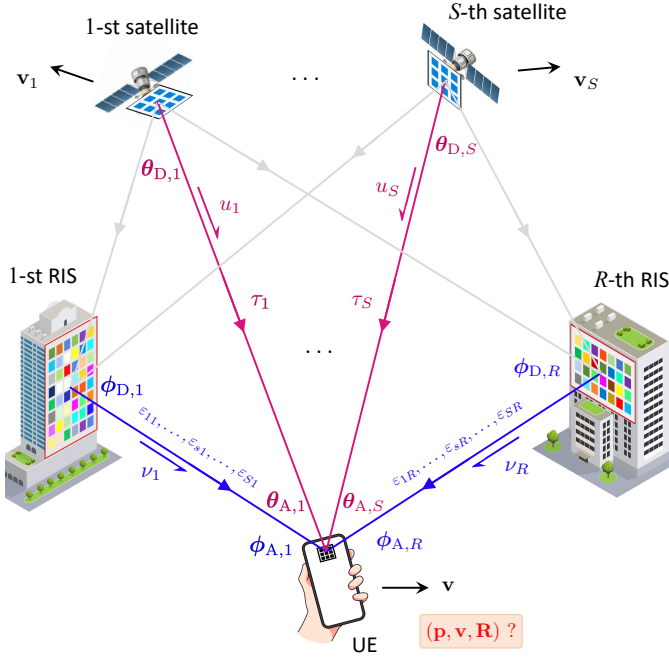


Fig. 1. Illustration of the considered hybrid terrestrial-satellite system with S LEO satellites and R RISs.

affirm that the proposed Riemannian manifold-based UKF effectively preserves the $SO(3)$ constraint. This preservation leads to a notable enhancement in the UE orientation estimation, consequently improving position and velocity estimation accuracy. Furthermore, extensive testing under various levels of state and observation uncertainty underscores the robustness of our algorithm.

The rest of the paper is organized as follows: Section II delineates the system model that integrates LEO satellites and RISs, detailing the geometry model, the signal model, and the transmission pipeline. Section III sets up the dynamic state-space model of the UE's motion with the corresponding uncertainty representation. Based on the defined models, Section IV meticulously describes our proposed Riemannian manifold-based tracking method, elucidating its components, operational dynamics, and algorithm details. The proposed system and algorithms are evaluated through a sequence of simulation tests in Section V. Finally, our conclusions are presented in Section VI.

II. SYSTEM MODEL

We consider a 9D user tracking problem in a hybrid terrestrial-satellite system consisting of S LEO satellites and R RISs, as depicted in Fig. 1. In this system, an unknown moving UE receives downlink signals from both satellite-UE direct channels and satellite-RIS-UE reflection channels and then performs a 9D self-tracking, capturing the 3D position, the 3D velocity, and the 3D orientation of the UE simultaneously. This section initially introduces the fundamental geometric relationship present in the system under consideration, followed by the signal model employed. Subsequently, we detail the timing framework for signal transmission and user tracking.

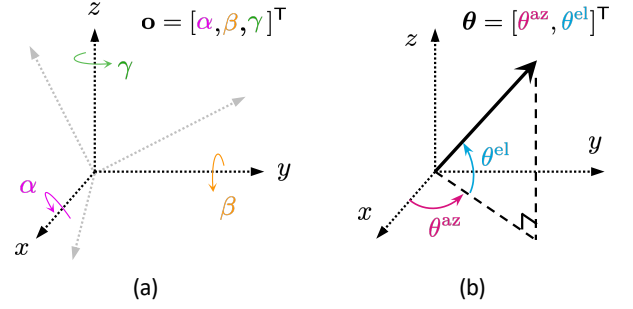


Fig. 2. Illustration of the geometric setups related to coordinate systems. (a) The definition of the Euler angles α , β , and γ . (b) The definition of the azimuth angle θ^{az} and the elevation angle θ^{el} .

A. Geometry Model

Within the proposed framework, the observation of the user tracking task is the geometric channel parameters, which are related to the user's position, velocity, and orientation through the geometric relationship. Therefore, this subsection presents the geometry model of the considered system and clarifies the underlying channel parameters, based on which the tracking algorithm will be developed further ahead.

Suppose the states of all the satellites and RISs are known when tracking the UE. The known position and velocity of the s -th LEO satellite is denoted by $\mathbf{p}_s \in \mathbb{R}^3$ and $\mathbf{v}_s \in \mathbb{R}^3$, respectively, while its orientation is represented by a rotation matrix $\mathbf{R}_s \in SO(3)$. Here, $SO(3)$ stands for the group of 3D rotations defined as

$$SO(3) \triangleq \{\mathbf{R} | \mathbf{R}^T \mathbf{R} = \mathbf{I}_3, \det(\mathbf{R}) = 1\}. \quad (1)$$

Specifically, the matrix \mathbf{R}_s describes the rotational connection between the body coordinate system of the s -th satellite and the global coordinate system. For example, for arbitrary vector \mathbf{d} at the global coordinate system, we can express it at the s -th satellite's body coordinate system as $\mathbf{R}_s^T \mathbf{d}$. Note that the degree of freedom of rotation matrices is 3. Such rotational relationships can be determined by 3D Euler angles $\{\alpha, \beta, \gamma\}$, which are visualized in Fig. 2-(a) and have the transform relation as [10], [35]

$$\mathbf{R} = \begin{bmatrix} C_\alpha C_\beta & C_\alpha S_\beta S_\gamma - S_\alpha C_\gamma & C_\alpha S_\beta C_\gamma + S_\alpha S_\gamma \\ S_\alpha C_\beta & S_\alpha S_\beta S_\gamma + C_\alpha C_\gamma & S_\alpha S_\beta C_\gamma - C_\alpha S_\gamma \\ -S_\beta & C_\beta S_\gamma & C_\beta C_\gamma \end{bmatrix}. \quad (2)$$

Here, C_φ and S_φ ($\varphi \in \{\alpha, \beta, \gamma\}$) are shorthand notations for $\cos \varphi$ and $\sin \varphi$, respectively.

The known position and orientation of the r -th RIS are denoted as $\mathbf{p}_r \in \mathbb{R}^3$ and $\mathbf{R}_r \in SO(3)$, respectively. Similarly, we denote the unknown position, velocity, and orientation of the UE as $\mathbf{p} \in \mathbb{R}^3$, $\mathbf{v} \in \mathbb{R}^3$, and $\mathbf{R} \in SO(3)$, respectively. Therefore, $(\mathbf{p}, \mathbf{v}, \mathbf{R})$ represent the total unknown UE state to be estimated. In this work, we assume the position and orientation of all RISs remain fixed over time, while the states of the UE and satellites undergo dynamic changes. For notational convenience, we temporarily omit time indexes from these variables and reintroduce them starting from Section III.

In this work, we assume downlink MIMO transmissions from LEO satellites to the UE with the reflection through

RISs. Let M_s , M_r , and M denote the number of antennas at the s -th LEO satellite, the r -th RIS, and the UE, respectively. Typically, several channel parameters related to the UE's state can be extracted through the channel estimation process based on the received signals from each of these MIMO channels. Therefore, we now define the involved channel parameters and clarify the geometric relationship between these channel parameters and the UE's state. Note that these channel parameters are associated with the corresponding LoS paths.²

1) *The Satellite-UE Direct Channel:* Taking the direct channel between the s -th satellite and the UE as an example, we investigate the channel parameters including the Doppler frequency shift, the AoD at the satellite, the AoA at the UE, and the channel delay.

The Doppler shift: We denote the Doppler shift observed from the channel between the s -th satellite and the UE as $u_s \in \mathbb{R}$, which can be defined as

$$u_s = \frac{(\mathbf{v}_s - \mathbf{v})^\top (\mathbf{p} - \mathbf{p}_s)}{\lambda \|(\mathbf{p} - \mathbf{p}_s)\|_2}. \quad (3)$$

Here, λ is the wavelength of the center frequency.

The AoD at satellite: The AoD at the s -th satellite is denoted by $\boldsymbol{\theta}_{D,s} \in \mathbb{R}^2$. Note that in 3D space, each AoD (or AoA) here consists of an azimuth angle and an elevation angle. i.e., $\boldsymbol{\theta}_{D,s} = [\theta_{D,s}^{\text{az}}, \theta_{D,s}^{\text{el}}]^\top$. The definition of the azimuth and elevation angles are presented in Fig. 2-(b). According to the underlying geometric relationship, these AoDs can be expressed in terms of the satellite and UE states as

$$\theta_{D,s}^{\text{az}} = \text{atan2}([\mathbf{R}_s^\top (\mathbf{p} - \mathbf{p}_s)]_2, [\mathbf{R}_s^\top (\mathbf{p} - \mathbf{p}_s)]_1), \quad (4)$$

$$\theta_{D,s}^{\text{el}} = \text{asin}([\mathbf{R}_s^\top (\mathbf{p} - \mathbf{p}_s)]_3 / \|\mathbf{p} - \mathbf{p}_s\|_2). \quad (5)$$

The AoA at UE: The AoA observed at the UE for the signals transmitted from the s -th satellite is denoted by $\boldsymbol{\theta}_{A,s} = [\theta_{A,s}^{\text{az}}, \theta_{A,s}^{\text{el}}]^\top \in \mathbb{R}^2$. Analogously, these AoAs can be expressed as

$$\theta_{A,s}^{\text{az}} = \text{atan2}([\mathbf{R}^\top (\mathbf{p}_s - \mathbf{p})]_2, [\mathbf{R}^\top (\mathbf{p}_s - \mathbf{p})]_1), \quad (6)$$

$$\theta_{A,s}^{\text{el}} = \text{asin}([\mathbf{R}^\top (\mathbf{p}_s - \mathbf{p})]_3 / \|\mathbf{p}_s - \mathbf{p}\|_2). \quad (7)$$

The channel delay: In addition, we denote the time delay of the channel between the s -th satellite and the UE as $\tau_s \in \mathbb{R}$, which can be expressed as

$$\tau_s = \frac{\|\mathbf{p}_s - \mathbf{p}\|_2}{c} + b_s, \quad (8)$$

where b_s is an unknown but fixed clock bias between the s -th LEO satellite and the UE.

2) *The Satellite-RIS-UE Reflection Channel:* As demonstrated in Fig. 1, there are $S \times R$ different satellite-RIS-UE channels. However, these reflection channels share the same R RIS-UE subchannels. Moreover, since the states of both LEO satellites and RISs are known, the informative channel parameters related to the UE state are concentrated in the R RIS-UE subchannels only. Taking the subchannel between the r -th RIS and the UE as an example, we can

similarly express the channel parameters in terms of the RIS and UE states.

The Doppler shift: The Doppler shift observed from the signals reflected through the r -th RIS is denoted as ν_r , which can be defined as

$$\nu_r = \frac{\mathbf{v}^\top (\mathbf{p}_r - \mathbf{p})}{\lambda \|(\mathbf{p}_r - \mathbf{p})\|_2}. \quad (9)$$

The AoD at RIS: The AoD at the r -th RIS is denoted as $\boldsymbol{\phi}_{D,r} = [\phi_{D,r}^{\text{az}}, \phi_{D,r}^{\text{el}}]^\top \in \mathbb{R}^2$ and is given by

$$\phi_{D,r}^{\text{az}} = \text{atan2}([\mathbf{R}_r^\top (\mathbf{p} - \mathbf{p}_r)]_2, [\mathbf{R}_r^\top (\mathbf{p} - \mathbf{p}_r)]_1), \quad (10)$$

$$\phi_{D,r}^{\text{el}} = \text{asin}([\mathbf{R}_r^\top (\mathbf{p} - \mathbf{p}_r)]_3 / \|\mathbf{p} - \mathbf{p}_r\|_2). \quad (11)$$

The AoA at UE: The AoA observed at the UE for the signals reflected through the r -th RIS is denoted as $\boldsymbol{\phi}_{A,r} = [\phi_{A,r}^{\text{az}}, \phi_{A,r}^{\text{el}}]^\top \in \mathbb{R}^2$ and is given by

$$\phi_{A,r}^{\text{az}} = \text{atan2}([\mathbf{R}^\top (\mathbf{p}_r - \mathbf{p})]_2, [\mathbf{R}^\top (\mathbf{p}_r - \mathbf{p})]_1), \quad (12)$$

$$\phi_{A,r}^{\text{el}} = \text{asin}([\mathbf{R}^\top (\mathbf{p}_r - \mathbf{p})]_3 / \|\mathbf{p}_r - \mathbf{p}\|_2). \quad (13)$$

The channel delay: Finally, we define the time delay of the subchannel between the r -th RIS and the UE. Note that in these reflection channels, the signals transmitted from different satellites possess different channel delays. To distinguish this, we denote the time delay observed at the signals transmitted from the s -th satellite and through the r -th RIS as ε_{sr} , which is defined as³

$$\varepsilon_{sr} = \frac{\|\mathbf{p}_r - \mathbf{p}\|_2}{c} + b_s. \quad (14)$$

B. Signal Model

For each LEO satellite, we consider a downlink pilot transmission with K subcarriers. Assume all the LEO satellites and the UE are equipped with a single radio-frequency chain (RFC). The received baseband signal at the UE from the s -th LEO satellite for the k -th subcarrier can be expressed as

$$y_s^k = \sqrt{P_s} \mathbf{w}_s^\top \bar{\mathbf{H}}_s^k \mathbf{f}_s x_s^k + n_s^k, \quad (15)$$

where $P_s \in \mathbb{R}$ denotes the average transmission power of the s -th LEO satellite, $\mathbf{w}_s \in \mathbb{C}^M$ the combiner, $\bar{\mathbf{H}}_s^k \in \mathbb{C}^{M \times M_s}$ the wireless channel between the s -th satellite and the UE, $\mathbf{f}_s \in \mathbb{C}^{M_s}$ the precoder, x_s^k the transmitted unit-modulus symbol, and $n_s^k \sim \mathcal{CN}(0, \sigma^2)$ the additive white Gaussian noise (AWGN). Note that here we utilize analog precoders and combiners.

The wireless channel $\bar{\mathbf{H}}_s^k$ can be decomposed as

$$\bar{\mathbf{H}}_s^k = \mathbf{H}_s^k + \sum_{r=1}^R \mathbf{H}_r^k \boldsymbol{\Gamma}_r \mathbf{H}_{sr}^k, \quad (16)$$

where $\mathbf{H}_s^k \in \mathbb{C}^{M \times M_s}$, $\mathbf{H}_{sr}^k \in \mathbb{C}^{M_r \times M_s}$, and $\mathbf{H}_r^k \in \mathbb{C}^{M \times M_r}$ represent the channel between the s -th satellite and the UE, the channel between the s -th satellite and the r -th RIS, and the channel between the r -th RIS and the UE, respectively. Here, $\boldsymbol{\Gamma}_r \in \mathbb{C}^{M_r \times M_r}$ is the reconfigurable reflection matrix

²In this work, we only utilize the channel parameters within the LoS paths to perform user tracking, while the multipath effect is treated as additive noise.

³Note that since the states of LEO satellites and RISs are known, the propagation delays over the satellite-RIS subchannels are known. Therefore, these parts of the delay are ignored in ε_{sr} .

of the r -th RIS, which is a diagonal matrix and assumed frequency-independent. The diagonal entry $\Gamma_r(i, i)$ stands for the reflection coefficient of the i -th unit cell in the RIS. Typically, a passive RIS keeps $|\Gamma_r(i, i)| \leq 1$, while an active RIS can provide an extra amplitude gain so that $|\Gamma_r(i, i)| > 1$, $\forall i = 1, \dots, M_R$.

Now we focus on the direct satellite-UE channel \mathbf{H}_s^k , which can be expressed as

$$\begin{aligned} \mathbf{H}_s^k &= \sum_{i=0}^{I_s} \mathbf{H}_s^k(i) \\ &= \sum_{i=0}^{I_s} \alpha_s^i e^{j2\pi(tu_s^i - k\Delta f\tau_s^i)} \mathbf{a}(\theta_{A,s}^i) \mathbf{a}_s^T(\theta_{D,s}^i), \end{aligned} \quad (17)$$

where i indexes the multipath channels with a LoS path and I_s non-line-of-sight (NLoS) paths. Here, α_s^i denotes the i -th complex channel gain, t denotes the time elapsed since the first transmission from the s -th satellite, $\Delta f = B/K$ is the subcarrier spacing with B denoting the signal bandwidth, and \mathbf{a} and \mathbf{a}_s represent the array response vectors of the UE and the s -th LEO satellite, respectively. Among the multipaths, the case $i = 0$ corresponds to the LoS channel, while the remaining indices represent NLoS multipath channels reflected by unknown scattering points (SPs). As a result, the parameters u_s^0 , τ_s^0 , $\theta_{A,s}^0$, and $\theta_{D,s}^0$ in (17) correspond to the channel parameters u_s , τ_s , $\theta_{A,s}$, and $\theta_{D,s}$ defined in Section II-A. This notation correspondence is consistently employed for subsequent discussions.

Analogously, the RIS-UE channel \mathbf{H}_r^k and the satellite-RIS channel \mathbf{H}_{sr}^k can be respectively expressed as

$$\begin{aligned} \mathbf{H}_r^k &= \sum_{i=0}^{I_r} \mathbf{H}_r^k(i) \\ &= \sum_{i=0}^{I_r} \alpha_r^i e^{j2\pi(t\nu_r^i - k\Delta f\epsilon_{sr}^i)} \mathbf{a}(\phi_{A,r}^i) \mathbf{a}_r^T(\phi_{D,r}^i), \\ \mathbf{H}_{sr}^k &= \alpha_{sr} e^{j2\pi(t\nu_{sr} - k\Delta f\epsilon_{sr})} \mathbf{a}(\varphi_{A,sr}) \mathbf{a}_s^T(\varphi_{D,sr}). \end{aligned} \quad (18)$$

Here, we assume there exists I_r NLoS paths in the channel between the r -th RIS and the UE. For the satellite-RIS channel, however, we assume the RISs are deployed at elevated positions that are far away from the near-ground clutters and thus there is no NLoS path between the satellite and RIS. In addition, the parameters ν_{sr} , ϵ_{sr} , $\varphi_{A,sr}$, and $\varphi_{D,sr}$, which respectively denote the Doppler shift, time delay, AoA, and AoD of the satellite-RIS channel, are assumed to be known since the state of both the LEO satellites and RISs are known.

C. Transmission and Tracking Framework

The temporal framework of the proposed tracking system is presented in Fig. 3. Let T_U denote the update interval of the moving UE's state estimation. We segment the tracking operation at each interval period into two sequential phases: Phase I for signal transmission and Phase II for state updates.

In Phase I, each of the LEO satellites first transmits G pilot symbols (each with symbol duration T) to the UE. For the g -th transmission, the time t in (17) and (18) is given by

$$t = (g-1)T, \quad g = 1, 2, \dots, G. \quad (19)$$

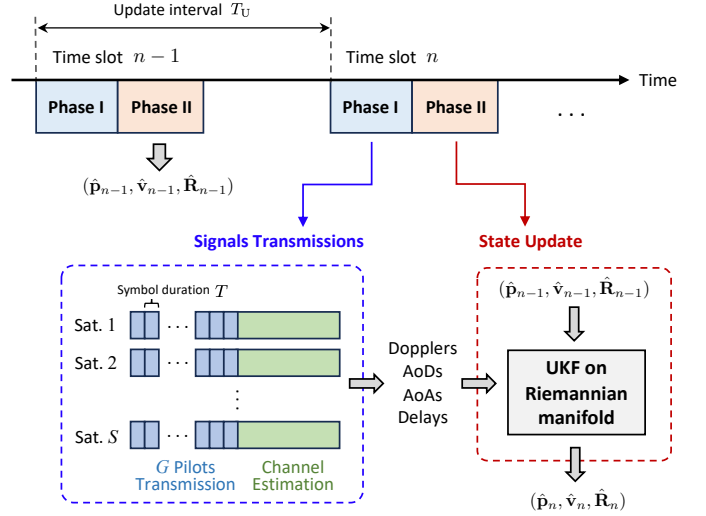


Fig. 3. The frame structure of the proposed hybrid tracking system.

We assume that the G transmissions are completed within the channel coherence time, ensuring that the position, velocity, and orientation of the UE remain constant. Furthermore, we adopt orthogonal frequency division for different satellites so that multiple satellites can transmit simultaneously. After the pilot transmissions of each satellite, a channel estimation process is conducted to obtain the geometric channel parameters including Doppler shifts, AoDs, AoAs, and channel delays, as elaborated in Section II-A.

In Phase II, we estimate and update the UE's 9D state based on 1) the geometric channel parameters collected from Phase I and 2) the UE state estimate at the previous time slot. As a foundation to develop the methodology, Section III comprehensively elucidates the dynamic state-space model governing the movement of the UE. Subsequently, Section IV will showcase how the proposed UKF, leveraging the Riemannian manifold, adeptly solves the state update problem under consideration.

III. DYNAMIC STATE-SPACE MODEL

Based on the system model described in Section II, the dynamic state-space model is presented in this section. We first clarify the time and measurement update relationships and then determine the underlying uncertainty representation.

A. Discrete-Time State-Space Dynamics

To formulate the tracking problem, we define the unknown state as

$$\zeta = [\mathbf{p}^T, \mathbf{v}^T, \mathbf{b}^T, \text{vec}(\mathbf{R})^T]^T \in \mathbb{R}^{S+15}, \quad (20)$$

where $\mathbf{b} = [b_1, b_2, \dots, b_S]^T \in \mathbb{R}^S$ is the unknown clock bias between the satellites and UE. The observations, on the other hand, are the geometric channel parameters defined in Section II-A, which we can concatenate as

$$\rho = [\rho_0^T, \rho_1^T, \dots, \rho_S^T]^T, \quad (21)$$

where

$$\boldsymbol{\rho}_0 = [\boldsymbol{\nu}^\top, \boldsymbol{\phi}_D^\top, \boldsymbol{\phi}_A^\top]^\top \in \mathbb{R}^{5R}, \quad (22)$$

$$\boldsymbol{\rho}_s = [u_s, \boldsymbol{\theta}_{D,s}^\top, \boldsymbol{\theta}_{A,s}^\top, \tau_s, \varepsilon_{s1}, \dots, \varepsilon_{sr}, \dots, \varepsilon_{sR}]^\top \in \mathbb{R}^{R+6}, \quad (23)$$

$$\boldsymbol{\nu} = [\nu_1, \dots, \nu_r, \dots, \nu_R]^\top \in \mathbb{R}^R, \quad (24)$$

$$\boldsymbol{\phi}_D = [\boldsymbol{\phi}_{D,1}^\top, \dots, \boldsymbol{\phi}_{D,r}^\top, \dots, \boldsymbol{\phi}_{D,R}^\top]^\top \in \mathbb{R}^{2R}, \quad (25)$$

$$\boldsymbol{\phi}_A = [\boldsymbol{\phi}_{A,1}^\top, \dots, \boldsymbol{\phi}_{A,r}^\top, \dots, \boldsymbol{\phi}_{A,R}^\top]^\top \in \mathbb{R}^{2R}. \quad (26)$$

Now we add the time indexes to the state vector $\boldsymbol{\zeta}$ and the observation vector $\boldsymbol{\rho}$. Thus the observations across a series of discrete time instants can be denoted as $\{\boldsymbol{\rho}_0, \boldsymbol{\rho}_1, \dots, \boldsymbol{\rho}_N\}$, and the corresponding states are denoted as $\{\boldsymbol{\zeta}_0, \boldsymbol{\zeta}_1, \dots, \boldsymbol{\zeta}_N\}$. Then, we can consider the following nonlinear dynamic system

$$\text{Time update: } \boldsymbol{\zeta}_{n+1} = f(\boldsymbol{\zeta}_n), \quad (27)$$

$$\text{Measurement update: } \boldsymbol{\rho}_n = h(\boldsymbol{\zeta}_n). \quad (28)$$

Here, $f(\cdot)$ is the process function and $h(\cdot)$ is the observation function.

1) *Process Function*: The process function $f(\cdot)$ is represented by the following mapping relationships:

$$\begin{aligned} \mathbf{p}_{n+1} &= \mathbf{p}_n + \mathbf{v}_n \delta_t + \tilde{\mathbf{a}}_n \frac{\delta_t^2}{2}, \\ \mathbf{v}_{n+1} &= \mathbf{v}_n + \tilde{\mathbf{a}}_n \delta_t, \\ \mathbf{b}_{n+1} &= \mathbf{b}_n, \\ \mathbf{R}_{n+1} &= \mathbf{R}_n \tilde{\boldsymbol{\Omega}}_n, \end{aligned} \quad (29)$$

where δ_t is the time interval between consecutive observations, $\tilde{\mathbf{a}}_n$ and $\tilde{\boldsymbol{\Omega}}_n$ are the UE's acceleration and rotation at the n -th time instant. For clarification, we can rewrite (27) as $\boldsymbol{\zeta}_{n+1} = f(\boldsymbol{\zeta}_n; \tilde{\mathbf{a}}_n, \tilde{\boldsymbol{\Omega}}_n)$. We assume that we can acquire a measurement of $\tilde{\mathbf{a}}_n$ and $\tilde{\boldsymbol{\Omega}}_n$ at each time instant through an inertial measurement unit (IMU) in the UE, which we can denote as

$$\hat{\mathbf{a}}_n = \tilde{\mathbf{a}}_n + \tilde{\mathbf{a}}_n \quad (30)$$

$$\hat{\boldsymbol{\Omega}}_n = \tilde{\boldsymbol{\Omega}}_n \tilde{\boldsymbol{\Omega}}_n, \quad (31)$$

where $\tilde{\mathbf{a}}_n$ and $\tilde{\boldsymbol{\Omega}}_n$ represent measurement errors that introduce perturbations on the state update.

2) *Observation Function*: The observation function maps the unknown UE state to the observed channel parameters, which are represented by (3)–(14). These channel parameters are, in turn, obtained by applying a channel estimation procedure and typically with certain estimation errors [36], [37].

B. Uncertainty Representation

Before developing our tracking algorithm, it is essential to determine the statistics of the uncertainty in the time update and the measurement update. Specifically, we can rewrite (27) and (28) as

$$\text{Time update: } \boldsymbol{\zeta}_{n+1} = f(\boldsymbol{\zeta}_n; \hat{\mathbf{a}}_n, \hat{\boldsymbol{\Omega}}_n) + \Delta \boldsymbol{\zeta}_{n+1}, \quad (32)$$

$$\text{Measurement update: } \hat{\boldsymbol{\rho}}_n = h(\boldsymbol{\zeta}_n) + \Delta \boldsymbol{\rho}_n, \quad (33)$$

where $\Delta \boldsymbol{\zeta}_{n+1}$ is the perturbation on the updated state introduced by the measurement errors $\tilde{\mathbf{a}}_n$ and $\tilde{\boldsymbol{\Omega}}_n$, and $\Delta \boldsymbol{\rho}_n$ stands for the estimation error of the channel parameters $\hat{\boldsymbol{\rho}}_n$. Now we determine the statistics of $\Delta \boldsymbol{\zeta}_{n+1}$ and $\Delta \boldsymbol{\rho}_n$, respectively.

1) *Uncertainty on Time Update*: We assume that the error on the acceleration measurement is an additive Gaussian noise $\tilde{\mathbf{a}}_n = \hat{\mathbf{a}}_n - \tilde{\mathbf{a}}_n \sim \mathcal{N}(\mathbf{0}, \mathbf{C}_a)$. For the error on the rotation measurement, we model a small perturbation using a similar routine as [33]. First, we define a 3D Gaussian vector $\tilde{\boldsymbol{\omega}}_n \sim \mathcal{N}(\mathbf{0}, \mathbf{C}_\omega)$. Then, the rotational perturbation $\tilde{\boldsymbol{\Omega}}_n$ is modeled as a small rotation around axis $\tilde{\boldsymbol{\omega}}_n \in \mathbb{R}^3$ with angle $\|\tilde{\boldsymbol{\omega}}_n\|$. We will detail this operation in Section IV-A. We assume that the covariance matrices of the IMU measurements, i.e., \mathbf{C}_a and \mathbf{C}_ω , are known.

Based on (29), the perturbation source to each component of the state vector $\boldsymbol{\zeta}_{n+1}$, i.e., $(\mathbf{p}_{n+1}, \mathbf{v}_{n+1}, \mathbf{b}_{n+1}, \mathbf{R}_{n+1})$, is $(\tilde{\mathbf{a}}_n \delta_t^2/2, \tilde{\mathbf{a}}_n \delta_t, \mathbf{0}_{S \times 1}, \tilde{\boldsymbol{\omega}}_n)$. When applying the classical UKF without considering SO(3) constraint, we can assign a Gaussian belief to the state as

$$\Delta \boldsymbol{\zeta}_{n+1} \sim \mathcal{N}(\mathbf{0}, \mathbf{S}), \quad (34)$$

where

$$\mathbf{S} = \begin{bmatrix} \frac{\delta_t^4}{4} \mathbf{C}_a & \frac{\delta_t^3}{2} \mathbf{C}_a & \mathbf{0}_{3 \times S} & \mathbf{0}_{3 \times 9} \\ \frac{\delta_t^3}{2} \mathbf{C}_a & \delta_t^2 \mathbf{C}_a & \mathbf{0}_{3 \times S} & \mathbf{0}_{3 \times 9} \\ \mathbf{0}_{S \times 3} & \mathbf{0}_{S \times 3} & \mathbf{0}_{S \times S} & \mathbf{0}_{S \times 9} \\ \mathbf{0}_{9 \times 3} & \mathbf{0}_{9 \times 3} & \mathbf{0}_{9 \times S} & \frac{\|\mathbf{C}_\omega\|_F}{2\pi} \mathbf{I}_9 \end{bmatrix} \in \mathbb{R}^{(S+15) \times (S+15)}. \quad (35)$$

Note that this covariance matrix is an approximation that may cause performance loss since the perturbation on the UE rotation is indeed not an additive variation. We will demonstrate that employing Riemannian manifold techniques can circumvent this approximation loss.

2) *Uncertainty on Measurement Update*: For the measurement update (33), the uncertainty $\Delta \boldsymbol{\rho}_n$ comes from the estimation error of the channel parameters $\boldsymbol{\rho}_n$. We assume that the required channel parameters are obtained through an efficient channel estimator. It then follows that the covariance matrix of $\Delta \boldsymbol{\rho}_n$ is given by the inverse of the Fisher information matrix (FIM) of the underlying channel estimation problem [38], [39].

To derive the FIM, let's rewrite the received signal y_s^k given in (15) as follows

$$y_s^k = \ell_s^k + z_s^k + n_s^k, \quad (36)$$

where ℓ_s^k is the received signal propagating through the LoS paths, and z_s^k contains all the NLoS multipath components. Based on the signal model in Section II-B, we have

$$\frac{\ell_s^k}{\sqrt{P_s} x_s^k} = \mathbf{w}_s^\top \left[\mathbf{H}_s^k(0) + \sum_{r=1}^R \mathbf{H}_r^k(0) \boldsymbol{\Gamma}_r \mathbf{H}_{sr}^k \right] \mathbf{f}_s, \quad (37)$$

$$\frac{z_s^k}{\sqrt{P_s} x_s^k} = \mathbf{w}_s^\top \left[\sum_{i=1}^{I_s} \mathbf{H}_s^k(i) + \sum_{r=1}^R \sum_{i=1}^{I_r} \mathbf{H}_r^k(i) \boldsymbol{\Gamma}_r \mathbf{H}_{sr}^k \right] \mathbf{f}_s. \quad (38)$$

With both LoS and NLoS paths present, the shadowed Rician model can be utilized to capture the statistics of the mixed channels, which aligns well with measurements and has been widely adopted in satellite channel modeling [40]–[42]. Typically, the Rician fading model treats the NLoS component of the received signal as a zero-mean Gaussian random variable while the LoS component is deterministic. The Rician fading is described in terms of a fading factor K_f , which is defined as the ratio of the LoS signal power to

the average power of the NLoS multipath signals [43]. Thus we have $z_s^k \sim \mathcal{CN}(0, |\ell_s^k|^2/K_f)$. Furthermore, since this work does not investigate the UE information from the NLoS signals, we treat z_s^k as an additive interference. Hence, we can combine the NLoS component z_s^k and the noise term n_s^k as $\tilde{n}_s^k = z_s^k + n_s^k \sim \mathcal{CN}(0, C_s^k)$, where $C_s^k = |\ell_s^k|^2/K_f + \sigma^2$. Therefore, we can rewrite (36) as

$$y_s^k = \ell_s^k + \tilde{n}_s^k. \quad (39)$$

Here, ℓ_s^k is the noise-free version of the received signal which the channel parameters are estimated from.

Based on model (39), the FIM of ρ , which is denoted as \mathbf{J} , can be computed using the steps outlined in Appendix A. Then we can write

$$\Delta \rho_n \sim \mathcal{N}(\mathbf{0}, \Sigma_n), \quad (40)$$

where $\Sigma_n = \mathbf{J}^{-1}(\zeta_n)$. Note that the computation of \mathbf{J} at time n requires the knowledge of the true UE state ζ_n , which is typically not available in the tracking process. To show this dependency, here we further detail the notation of the FIM as $\mathbf{J}(\zeta_n)$.

IV. THE PROPOSED UKF ON RIEMANNIAN MANIFOLD

Since the observation function is nonlinear, the UKF framework is chosen to solve the 9D tracking problem. The UKF is a variation of the Kalman filter, bypassing the necessity for linearization and derivative computation by approximating the first and second-order moments of the state via a cluster of sigma points [44], [45]. To handle the problems introduced by the constrained state and the unknown statistics of observations, this section proposes a novel Riemannian manifold-based 9D tracking method grounded on the UKF framework.

A. State Representation via Riemannian Manifold Geometry

As mentioned in Section III-B1, the classical UKF cannot preserve the SO(3) constraint on the UE orientation, which results in an inaccurate update of the state covariance matrix and degrades the estimation performance. To address this limitation, we employ the principles of Riemannian manifold theory. This theory offers a powerful toolset for navigating the smooth curvature of high-dimensional spaces and forces the states to fall into the constrained space. For a more comprehensive review of the Riemannian manifold, readers are directed to [46], [47].

By inspecting the state vector ζ in (20), we see the UE orientation \mathbf{R} lies in the group of 3D rotation SO(3), as defined in (1). SO(3) is a smooth and parallelizable Riemannian submanifold of the Euclidean space $\mathbb{R}^{3 \times 3}$ [34]. On the contrary, the other variables in ζ lie in the Euclidean space, which is also a Riemannian manifold. Specifically, we have

$$\mathbf{p} \in \mathbb{R}^3, \mathbf{v} \in \mathbb{R}^3, \mathbf{b} \in \mathbb{R}^S, \mathbf{R} \in \text{SO}(3). \quad (41)$$

Since the Cartesian product of two embedded submanifolds yields a new manifold, we define the following compound manifold

$$\mathbb{M} = \mathbb{R}^3 \times \mathbb{R}^3 \times \mathbb{R}^S \times \text{SO}(3), \quad (42)$$

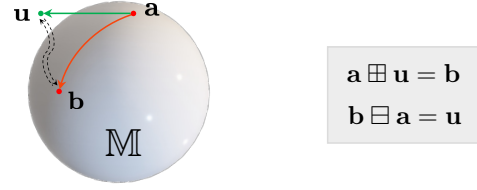


Fig. 4. Visualization of the defined \oplus and \ominus operations.

where \times represents the Cartesian product. According to the model in (29) and the analysis in Section III-B1, for each updated point $\zeta_{n+1} \in \mathbb{M}$, the corresponding perturbations are introduced by $(\tilde{\mathbf{a}}_n \delta_t^2/2, \tilde{\mathbf{a}}_n \delta_t, \mathbf{0}_{S \times 1}, \tilde{\omega}_n) \in \mathbb{R}^3 \times \mathbb{R}^3 \times \mathbb{R}^S \times \mathbb{R}^3$. To accurately characterize the perturbation introduction and keep the SO(3) constraint, we define the following two encapsulation operators [33], which are visualized in Fig. 4.

Definition 1 (\oplus operation): For a manifold \mathbb{F} , the \oplus operation combines a point $\mathbf{a} \in \mathbb{F}$ and a Euclidean vector $\mathbf{u} \in \mathbb{R}^n$ to produce another point $\mathbf{b} = \mathbf{a} \oplus \mathbf{u} \in \mathbb{F}$.

Definition 2 (\ominus operation): For two points $\mathbf{a}, \mathbf{b} \in \mathbb{F}$ on a manifold \mathbb{F} , and given a Euclidean vector $\mathbf{u} \in \mathbb{R}^n$ such that $\mathbf{b} = \mathbf{a} \oplus \mathbf{u} \in \mathbb{F}$, the \ominus operation retrieves the Euclidean vector $\mathbf{u} = \mathbf{b} \ominus \mathbf{a} \in \mathbb{R}^n$.

Note that the defined operations \oplus and \ominus can be implemented in different ways. According to Definition 1, for arbitrary $(\mathbf{p}, \mathbf{v}, \mathbf{b}, \mathbf{R}) \in \mathbb{M}$ and $(\mathbf{e}_1, \mathbf{e}_2, \mathbf{e}_3, \mathbf{e}_4) \in \mathbb{R}^3 \times \mathbb{R}^3 \times \mathbb{R}^S \times \mathbb{R}^3$, one realization of \oplus is given by

$$(\mathbf{p}, \mathbf{v}, \mathbf{b}, \mathbf{R}) \oplus (\mathbf{e}_1, \mathbf{e}_2, \mathbf{e}_3, \mathbf{e}_4) = (\mathbf{p} + \mathbf{e}_1, \mathbf{v} + \mathbf{e}_2, \mathbf{b} + \mathbf{e}_3, \mathbf{R} \boxplus_{\text{SO}(3)} \mathbf{e}_4). \quad (43)$$

Here, $\mathbf{R} \boxplus_{\text{SO}(3)} \mathbf{e}_4$, as described in Section III-B1, denotes the operation that adds the rotation around axis $\mathbf{e}_4 \in \mathbb{R}^3$ with angle $\|\mathbf{e}_4\|$ to \mathbf{R} . Specifically, such operation can be conducted as [33], [48, Sec. 4]

$$\mathbf{R} \boxplus_{\text{SO}(3)} \mathbf{e}_4 = \mathbf{R} \mathbf{R}_4, \quad (44)$$

where

$$\mathbf{R}_4 = \cos \vartheta \mathbf{I}_3 + (1 - \cos \vartheta) \mathbf{a} \mathbf{a}^\top + \sin \vartheta \mathbf{B}, \quad (45)$$

$$\vartheta = \|\mathbf{e}_4\|, \quad \mathbf{a} = \mathbf{e}_4 / \|\mathbf{e}_4\|, \quad (46)$$

$$\mathbf{B} = \begin{bmatrix} 0 & -\mathbf{e}_4[3] & \mathbf{e}_4[2] \\ \mathbf{e}_4[3] & 0 & -\mathbf{e}_4[1] \\ -\mathbf{e}_4[2] & \mathbf{e}_4[1] & 0 \end{bmatrix}. \quad (47)$$

According to Definition 2, for arbitrary two points $(\mathbf{p}^a, \mathbf{v}^a, \mathbf{b}^a, \mathbf{R}^a)$ and $(\mathbf{p}^b, \mathbf{v}^b, \mathbf{b}^b, \mathbf{R}^b)$ in \mathbb{M} , we can implement

$$(\mathbf{p}^a, \mathbf{v}^a, \mathbf{b}^a, \mathbf{R}^a) \ominus (\mathbf{p}^b, \mathbf{v}^b, \mathbf{b}^b, \mathbf{R}^b) = (\mathbf{p}^a - \mathbf{p}^b, \mathbf{v}^a - \mathbf{v}^b, \mathbf{b}^a - \mathbf{b}^b, \mathbf{R}^a \boxminus_{\text{SO}(3)} \mathbf{R}^b). \quad (48)$$

Here, $\boxminus_{\text{SO}(3)}$ is the inverse operation of $\boxplus_{\text{SO}(3)}$, which is given by [33]

$$\mathbf{R}^a \boxminus_{\text{SO}(3)} \mathbf{R}^b = \frac{\varphi}{2 \sin \varphi} \begin{bmatrix} D_{3,2} - D_{2,3} \\ D_{1,3} - D_{3,1} \\ D_{2,1} - D_{1,2} \end{bmatrix}, \quad (49)$$

$$\varphi = \arccos \frac{\text{Tr}(\mathbf{D}) - 1}{2}, \quad \mathbf{D} = (\mathbf{R}^b)^\top \mathbf{R}^a. \quad (50)$$

Next, we will integrate these operations into the UKF framework to address the considered 9D tracking problem.

B. UKF on Riemannian Manifold

The defined operations \boxplus and \boxminus allow us to accurately capture the perturbation statistics. For each time instant n , we can re-denote perturbation $(\tilde{\mathbf{a}}_n \delta_t^2/2, \tilde{\mathbf{a}}_n \delta_t, \mathbf{0}_{S \times 1}, \tilde{\omega}_n) \in \mathbb{R}^3 \times \mathbb{R}^3 \times \mathbb{R}^S \times \mathbb{R}^3$ as $[\tilde{\mathbf{a}}_n \delta_t^2/2, \tilde{\mathbf{a}}_n \delta_t, \mathbf{0}_{S \times 1}, \tilde{\omega}_n]^\top \in \mathbb{R}^{S+9}$, whose statistics follows

$$[\tilde{\mathbf{a}}_n \delta_t^2/2, \tilde{\mathbf{a}}_n \delta_t, \mathbf{0}_{S \times 1}, \tilde{\omega}_n]^\top \sim \mathcal{N}(\mathbf{0}, \mathbf{P}), \quad (51)$$

where

$$\mathbf{P} = \begin{bmatrix} \frac{\delta_t^4}{4} \mathbf{C}_a & \frac{\delta_t^3}{2} \mathbf{C}_a & \mathbf{0}_{3 \times S} & \mathbf{0}_{3 \times 3} \\ \frac{\delta_t^3}{2} \mathbf{C}_a & \delta_t^2 \mathbf{C}_a & \mathbf{0}_{3 \times S} & \mathbf{0}_{3 \times 3} \\ \mathbf{0}_{S \times 3} & \mathbf{0}_{S \times 3} & \mathbf{0}_{S \times S} & \mathbf{0}_{S \times 3} \\ \mathbf{0}_{3 \times 3} & \mathbf{0}_{3 \times 3} & \mathbf{0}_{3 \times S} & \mathbf{C}_\omega \end{bmatrix} \in \mathbb{R}^{(S+9) \times (S+9)}. \quad (52)$$

Then, we can develop the sigma point propagation for the time update and the measurement update steps.

1) *Time Update*: Let $\tilde{\zeta}_{n-1}$ denote the mean of the state ζ_{n-1} at time $n-1$, and \mathbf{P}_{n-1} denote the corresponding covariance matrix of the perturbation. We can generate $2N_p+1$ sigma vectors according to the following

$$\begin{aligned} \mathbf{z}_0 &= \tilde{\zeta}_{n-1}, \\ \mathbf{z}_i &= \tilde{\zeta}_{n-1} \boxplus \left(\sqrt{(N_p + \Lambda) \mathbf{P}_{n-1}} \right)_i, \quad i = 1, \dots, N_p, \\ \mathbf{z}_{i+N_p} &= \tilde{\zeta}_{n-1} \boxplus \left(\sqrt{(N_p + \Lambda) \mathbf{P}_{n-1}} \right)_i, \quad i = 1, \dots, N_p, \end{aligned} \quad (53)$$

where $N_p = S+9$, the notation $(\sqrt{\mathbf{A}})_i$ denotes the i -th column of the square root of the matrix \mathbf{A} , and Λ is a parameter controlling the dispersion of the generated sigma points. The operation \boxplus guarantees that all generated sigma points lie on the defined manifold \mathbb{M} , and thus the state statistics can propagate ahead with the $\text{SO}(3)$ constraint.

Based on the propagation of these sigma points, the mean of the state at the time instant n can be predicted as

$$\tilde{\zeta}_n = \text{MoSP}(\{W_i^{(m)}\}, \{f(\mathbf{z}_i)\}), \quad (54)$$

Here, $\text{MoSP}(\cdot)$ is a function that returns the mean of a set of points on the defined manifold. An iterative practice for the mean computation on a manifold is provided in [33, Tab. 3]. Alternatively, such a mean on $\text{SO}(3)$ can also be obtained by calculating the Karcher mean [49]. Subsequently, the covariance matrix of the state estimate at the time instant n can be predicted as

$$\tilde{\mathbf{P}}_n = \sum_{i=0}^{2N_p} W_i^{(c)} (f(\mathbf{z}_i) \boxminus \tilde{\zeta}_n) (f(\mathbf{z}_i) \boxminus \tilde{\zeta}_n)^\top + \mathbf{P}, \quad (55)$$

where \mathbf{P} is given by (52), and $W_i^{(m)}$ and $W_i^{(c)}$ are the associated weights to the corresponding sigma point, which are typically set as⁴

$$\begin{aligned} W_0^{(m)} &= \frac{\Lambda}{N_p + \Lambda}, \\ W_0^{(c)} &= \frac{\Lambda}{N_p + \Lambda} + (1 - \alpha^2 + \beta), \\ W_i^{(m)} &= W_i^{(c)} = \frac{1}{2(N_p + \Lambda)}, \quad i = 1, 2, \dots, 2N_p, \\ \Lambda &= \alpha^2(N_p + \kappa) - N_p. \end{aligned} \quad (56)$$

2) *Measurement Update*: Based on the predicted state mean $\tilde{\zeta}_n$ and perturbation covariance matrix $\tilde{\mathbf{P}}_n$, we can further generate a set of sigma points to predict the first and second moments of the observation at time n . Specifically, we can generate $2N_p+1$ sigma vectors according to the following

$$\begin{aligned} \mathbf{x}_0 &= \tilde{\zeta}_n, \\ \mathbf{x}_i &= \tilde{\zeta}_n \boxplus \left(\sqrt{(N_p + \Lambda) \tilde{\mathbf{P}}_n} \right)_i, \quad i = 1, \dots, N_p, \\ \mathbf{x}_{i+N_p} &= \tilde{\zeta}_n \boxplus \left(\sqrt{(N_p + \Lambda) \tilde{\mathbf{P}}_n} \right)_i, \quad i = 1, \dots, N_p. \end{aligned} \quad (57)$$

Then, the mean vector and covariance matrix of the observation estimate at the time n can be predicted as

$$\tilde{\rho}_n = \sum_{i=0}^{2N_p} W_i^{(m)} h(\mathbf{x}_i), \quad (58)$$

$$\tilde{\mathbf{Q}}_n = \sum_{i=0}^{2N_p} W_i^{(c)} (h(\mathbf{x}_i) - \tilde{\rho}_n) (h(\mathbf{x}_i) - \tilde{\rho}_n)^\top + \Sigma_n. \quad (59)$$

Note that here Σ_n is the covariance matrix of the observation perturbation $\Delta \rho_n$ in (33). As demonstrated in (40), $\Sigma_n = \mathbf{J}^{-1}(\zeta_n)$. However, the true UE state ζ_n is typically unavailable. To address this, we propose to approximate Σ_n as follows

$$\hat{\Sigma}_n = \epsilon \mathbf{I} + \sum_{i=0}^{2N_p} W_i^{(c)} \mathbf{J}^{-1}(\mathbf{x}_i), \quad (60)$$

where ϵ is an empirical parameter and a smaller ϵ represents a higher level of trust in the calculated FIMs $\mathbf{J}(\mathbf{x}_i)$. Our simulation suggests that the value of ϵ should be adjusted according to the dimension of $\mathbf{J}(\mathbf{x}_i)$, which depends on the system configuration and the visibility of the UE to the RISs and satellites. Generally, when the dimension of $\mathbf{J}(\mathbf{x}_i)$ is higher, assigning a lower value to ϵ tends to yield better performance.

Next, we can compute the cross-covariance matrix between the predicted state and observation as

$$\tilde{\mathbf{Q}}_{\zeta\eta,n} = \sum_{i=0}^{2N_p} W_i^{(c)} (f(\mathbf{z}_i) \boxminus \tilde{\zeta}_n) (h(\mathbf{x}_i) - \tilde{\rho}_n)^\top. \quad (61)$$

Therefore, the Kalman gain is obtained as

$$\mathbf{K}_n = \tilde{\mathbf{Q}}_{\zeta\eta,n} \tilde{\mathbf{Q}}_n^{-1}. \quad (62)$$

⁴The parameters α , β , and κ need to be tuned. A popular choice is $\alpha = 0.001$, $\beta = 2$, and $\kappa = 0$.

Algorithm 1 9D Tracking Using Constrained UKF

Input: Observations $\{\hat{\rho}_n\}$.

Output: Hidden states estimates $\{\hat{\zeta}_n\}$.

- 1: Initialize with: $\hat{\zeta}_{-1} = \mathbb{E}\zeta_{-1}$ and $\hat{\mathbf{P}}_{-1} = \mathbf{0}_{(S+9) \times (S+9)}$.
 - 2: **for** $n \geq 0$ **do**
 - 3: — *Time Update:*
 - 4: Generate $2N_p + 1$ sigma points $\{\mathbf{z}_i\}$ and the corresponding weights $\{W_i^{(m)}, W_i^{(c)}\}$ according to (53) and (56).
 - 5: Obtain $\tilde{\zeta}_n$ and $\tilde{\mathbf{P}}_n$ according to (54) and (55).
 - 6: — *Measurement Update:*
 - 7: Generate $2N_p + 1$ sigma points $\{\mathbf{x}_i\}$ according to (57).
 - 8: Obtain $\tilde{\rho}_n$ and $\tilde{\mathbf{Q}}_n$ according to (58), (59), and (60).
 - 9: Compute the cross-covariance $\tilde{\mathbf{Q}}_{\zeta\eta,n}$ according to (61).
 - 10: Compute the Kalman gain \mathbf{K}_n according to (62).
 - 11: Obtain the estimates of the mean and covariance matrix of the hidden state $\hat{\zeta}_n$ and $\hat{\mathbf{P}}_n$ according to (63) and (64).
 - 12: **end for**
-

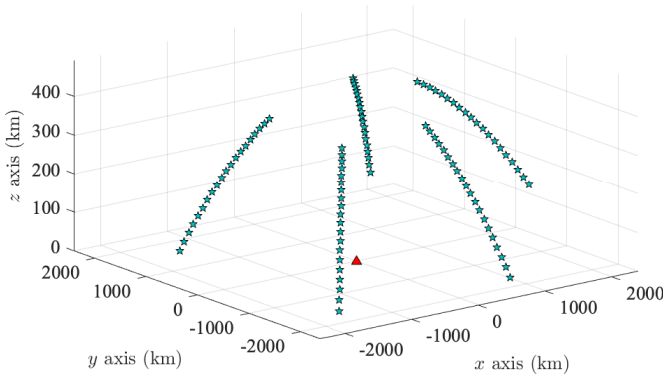


Fig. 5. The trajectory of the generated 5 LEO satellites during a 180-second observation. The red triangle indicates the area of interest.

Finally, we use the acquired observation vector $\hat{\rho}_n$ at the time n to correct the state estimation as

$$\hat{\zeta}_n = \tilde{\zeta}_n \boxplus \mathbf{K}_n(\hat{\rho}_n - \tilde{\rho}_n), \quad (63)$$

$$\hat{\mathbf{P}}_n = \tilde{\mathbf{P}}_n - \mathbf{K}_n \tilde{\mathbf{R}}_n \mathbf{K}_n^T. \quad (64)$$

The procedure of the proposed UKF method based on the Riemannian manifold is summarized in Algorithm 1.

V. NUMERICAL RESULTS

A. The Simulation Setup

During the simulations, we employ a Walker Star constellation of LEO satellites [19] with respect to the area of interest, as depicted in Fig. 5. The movements of the LEO satellites are simulated using the QuaDRiGa toolbox [50]. Meanwhile, the trajectory of the UE is depicted in Fig. 6, which is segmented into rural, suburban, and urban segments to reflect diverse environmental conditions. Different values of Rician fading factor K_f are allocated to the three environments, according

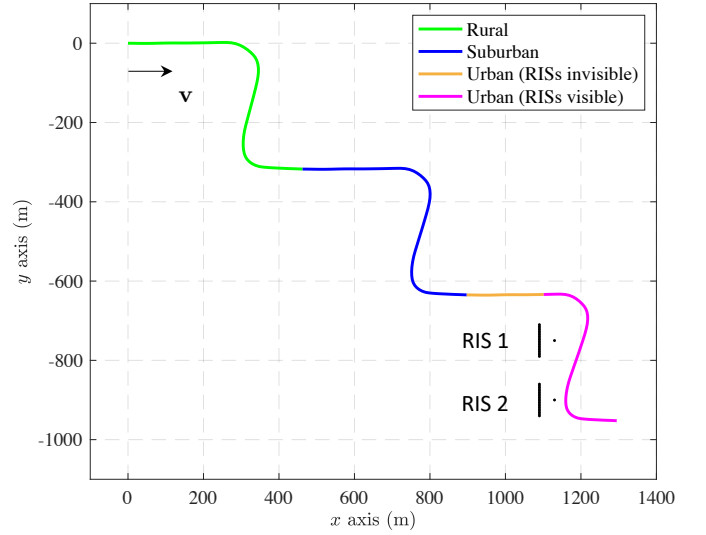


Fig. 6. The demonstration of the simulated UE trajectory traversing rural, suburban, and urban regions. Two RISs are deployed in the urban area, dividing it into two segments: the visible area and the invisible area of the RISs. Here, we use two dots to indicate the normal directions of the two RISs.

to the real measured results in [51]. In addition, two RISs are strategically deployed in the urban region, which further divides the urban area into two zones: 1) the RIS-visible area and 2) the RIS-invisible area.

Throughout the simulations, the channel gain is computed based on the large-scale path loss model provided in [52]. Specifically, the satellite-UE/RIS path loss is composed of components as follows:

$$\text{PL} = \text{FSPL} + \text{SF} + \text{CL} + \text{PL}_g + \text{PL}_s \text{ (dB)}, \quad (65)$$

where PL is the total path loss, FSPL is the free space path loss, SF is the shadow fading loss represented by a random Gaussian variable, CL is the clutter loss, PL_g is the attenuation due to atmospheric absorption, and PL_s is the attenuation due to either ionospheric or tropospheric scintillation. Typically, the clutter loss $\text{CL} = 0$ dB in the LoS condition and the ionospheric scintillation in PL_s can be ignored for frequencies above 6 GHz [52].

The free space path loss and shadow fading loss are calculated according to the method in [53] as

$$\text{FSPL}(d, f_c) = 32.45 + 20 \log_{10} d + 20 \log_{10} f_c \text{ (dB)}, \quad (66)$$

$$\text{SF}(\theta_{\text{SAT}}) = X(V_\sigma + V_\theta \log_{10} \theta_{\text{SAT}}) \text{ (dB)}, \quad (67)$$

where d represents the distance between the transmitter and receiver in meters, f_c denotes the carrier frequency in gigahertz (GHz), X is a Gaussian distributed random variable with zero-mean and unit variance, V_σ and V_θ are parameters varying from environments, and θ_{SAT} is the elevation angle of the satellite to the UE measured in radians. The selection of the values V_σ and V_θ are listed in Table I, based on the data provided in [53]. The atmospheric absorption PL_g depends on the signal frequency f_c and the satellite elevation angle θ_{SAT} . A detailed calculation method based on layered approximation has been provided by the International Telecommunication Union (ITU) in [54] and a MATLAB script is available in [55].

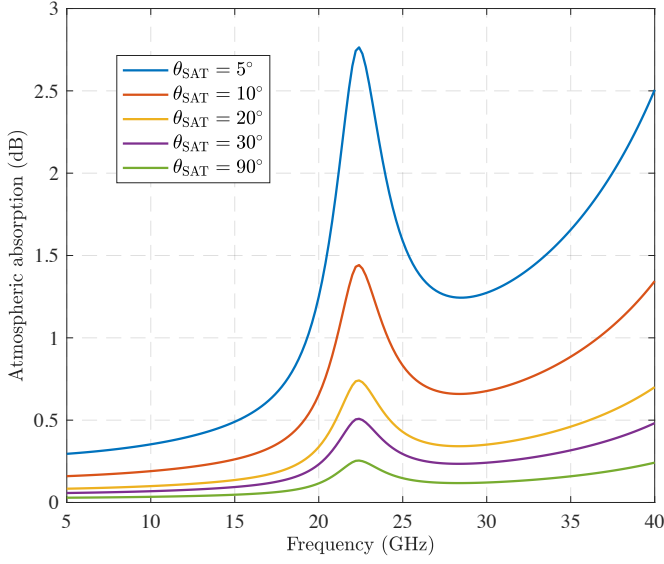


Fig. 7. The evaluation of the atmospheric absorption vs. signal frequency and satellite elevation angle, based on the computation method in [54], [55].

As an example, Fig. 7 presents the strength of the atmospheric absorption vs. signal frequency in several sample elevation angles. Generally, a lower elevation angle θ_{SAT} results in a higher atmospheric absorption PL_g . Since the tropospheric attenuation in PL_s is latitude-dependent, there is no generic analytic evaluation model. An illustrative example of the tropospheric scintillation attenuation at 20 GHz in Toulouse, France is provided in [52, Table 6.6.6.2.1-1], which is adopted as a reference in this work. Besides, while the path loss of the link between the satellite and UE/RIS is computed according to (65), the path loss of the link between the RIS and UE is obtained by keeping FSPL and SF only.

To conduct a more realistic evaluation, we further take the LoS probability into account. That is, we set the amplitude of the LoS channel gain as the expectation $P(\theta_{\text{SAT}})10^{-\text{PL}/20}$, where $P(\theta_{\text{SAT}})$ denotes the LoS probability. The value of $P(\theta_{\text{SAT}})$ varies across different environments based on the data provided in [52, Table 6.6.1-1], which is also summarized in Table I. Additionally, the phases of these channel gains are randomly generated through a uniform distribution between 0 and 2π [25], [28], [39].

The covariance matrices of the acceleration and rotation measurements are defined as $\mathbf{C}_a = \sigma_a^2 \mathbf{I}_3$ and $\mathbf{C}_\omega = \sigma_\omega^2 \mathbf{I}_3$. All the precoders, combiners, and RIS phase shifts are randomly assigned. Since it has been verified that active RISs can outperform passive RISs in terms of user positioning within the practical power supplies [28], we choose to deploy active RISs in our system during the following performance evaluation. We assume a power supply P_R to each active RIS, and the amplification coefficient of the RIS can be calculated following [28, Eq. (85)]. The clock bias between each satellite and the UE are randomly set between 80 ns and 120 ns, which is assumed fixed over the observation duration. Furthermore, we assume all the LEO satellites keep the same transmission power P_T . All the other default simulation parameters are summarized in Table II.

TABLE I
ENVIRONMENT-SPECIFIC PARAMETERS

Parameter	Rural	Suburban	Urban
V_σ	1.40	1.45	0.10
V_θ	1.00	0.85	0.00
$P(10^\circ)$	78.2 %		24.6 %
$P(20^\circ)$	86.9 %		38.6 %
$P(30^\circ)$	91.9 %		49.3 %
$P(40^\circ)$	92.9 %		61.3 %
$P(50^\circ)$	93.5 %		72.6 %
$P(60^\circ)$	94.0 %		80.5 %
$P(70^\circ)$	94.9 %		91.9 %
$P(80^\circ)$	95.2 %		96.8 %
$P(90^\circ)$	99.8 %		99.2 %

TABLE II
DEFAULT SIMULATION PARAMETERS

Parameter	Value
Number of LEO satellites S	5
Number of RISs R	2
Number of Subcarriers K	3000
Number of Transmissions G	32
Carrier Frequency f_c	12.7 GHz
Bandwidth B	240 MHz
Transmission Power P_T	50 dBm
Active RIS Power P_R	0 dBm
Noise PSD of Receiver & RIS	-174 dBm/Hz
Noise Figure of Receiver & RIS	0 dB
Array Size of satellite / RIS / UE	$4 \times 4 / 20 \times 20 / 4 \times 4$
Array Spacing of satellite / RIS / UE	5 mm / 5 mm / 5 mm
Rural / Suburban / Urban K_f [51]	3 dB / 2.6 dB / 1.85 dB
Acceleration standard deviation σ_a	0.2 m/s ²
Rotation standard deviation σ_ω	2 °
Update Interval T_U	1 s
Symbol Duration T	10 ms
Orbit Height of LEO satellites	500 km

B. 9D Tracking Performance Evaluation

1) *The Evaluation of the Proposed Belief Assignment Principle:* First, we evaluate the proposed belief assignment principle as formulated in (60). Fig. 8 presents the estimation errors of the UE position, velocity, and orientation during a 180-second tracking duration. In this simulation, we set $\epsilon = 0.5$ in the rural, suburban, and RIS-invisible urban regions, while set $\epsilon = 0$ in the RIS-visible urban areas. As benchmarks, we compared the proposed FIM-based belief approximation (60) with 1) the identical belief $\hat{\Sigma}_n = \mathbf{I}$ and 2) the true covariance matrix $\hat{\Sigma}_n = \mathbf{J}^{-1}(\zeta_n)$. Note that the true covariance matrix $\mathbf{J}^{-1}(\zeta_n)$ is typically unavailable in practice, and here we adopt it as a performance limit. It is clearly shown that while the true covariance matrix belief (blue curve) yields the best performance, the proposed belief assignment principle (60) (red curve) significantly outperforms the identical belief assignment (green curve). In particular, we can observe that the FIM approximation (60) can achieve performance comparable to that of the true covariance matrix in some regions, demonstrating the superiority of the proposed

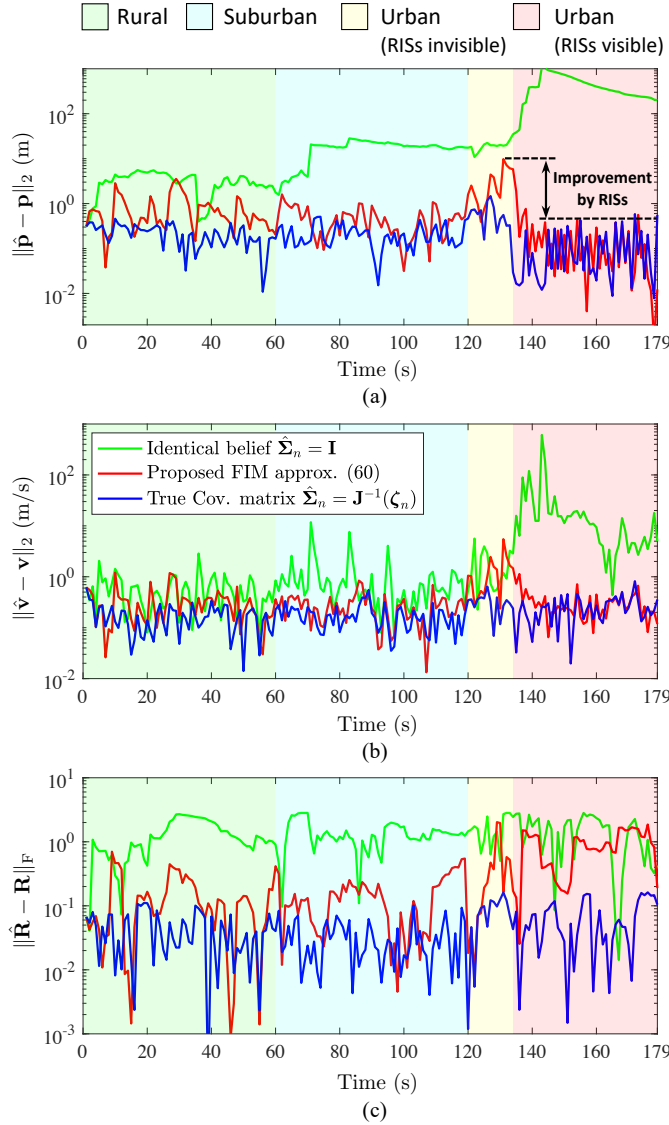


Fig. 8. The comparison of the estimation errors vs. time using different assignment principles of the belief $\hat{\Sigma}_n$. (a) Estimation errors of the UE position \mathbf{p} . (b) Estimation errors of the UE velocity \mathbf{v} . (c) Estimation errors of the UE orientation \mathbf{R} .

principle.

Another important observation is that the introduction of RISs can substantially improve the accuracy of the UE position estimation in the urban environment despite the lower Rician factor and channel gains, as highlighted in Fig. 8-(a). Meanwhile, it is also revealed that the inclusion of RISs can only be positive when an appropriate belief $\hat{\Sigma}_n$ is assigned. This can be observed from the identical belief (green curve) in Fig. 8-(a), where the tracking performance is even degraded when the RISs are introduced. In contrast, both the proposed FIM approximation and the true covariance matrix can make good use of the additional information introduced by RISs and gain substantial performance improvement for up to more than an order of magnitude. This reveals the potential of RISs in enhancing the tracking services based on LEO satellite signals. Such an improvement appears because the RISs can not only

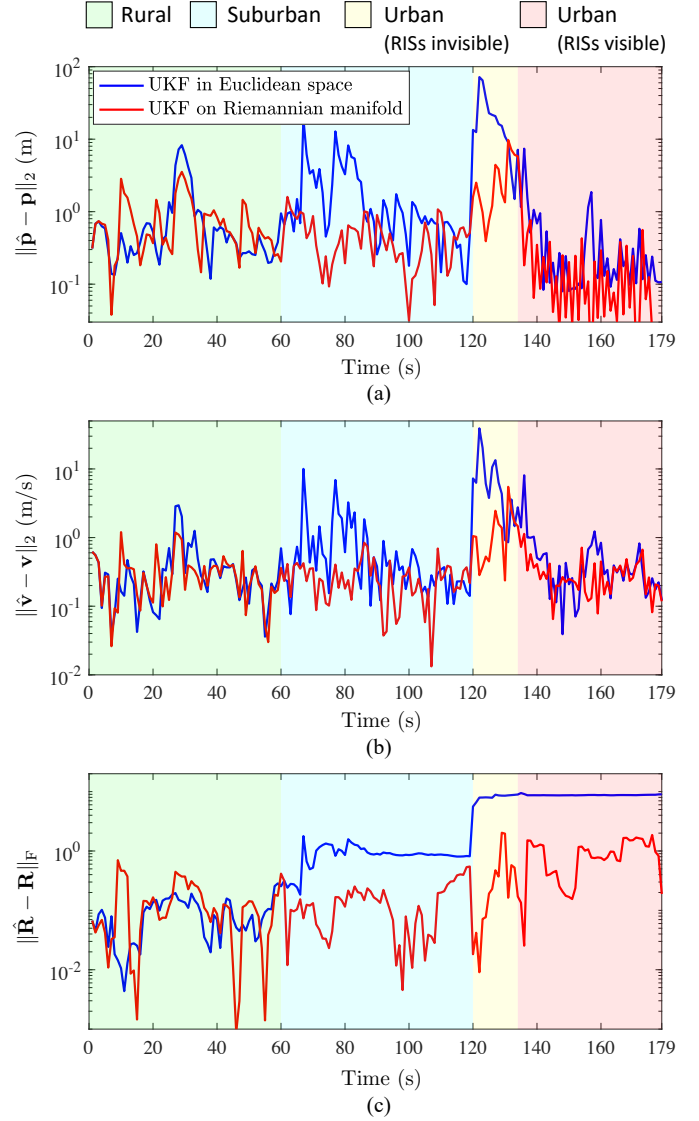


Fig. 9. The comparison of the estimation errors vs. time using the UKFs in Euclidean space and on Riemannian manifold. (a) Estimation errors of the UE position \mathbf{p} . (b) Estimation errors of the UE velocity \mathbf{v} . (c) Estimation errors of the UE orientation \mathbf{R} .

increase the received power of the satellite signals but also provide additional location references that help determine the UE's position [25], [27], [28]. When it comes to the velocity and orientation estimation, however, the introduction of RISs cannot enhance the estimation performance as effectively as the position estimation, see Fig. 8-(b) and Fig. 8-(c). Such a phenomenon can be explained by the geometry model in Section II-A. All the channel parameters related to the RIS reflection channels contain certain information about the UE position since all of them are the functions of \mathbf{p} . On the contrary, only part of these channel parameters are the functions of \mathbf{v} or \mathbf{R} . Therefore, introducing RISs benefits the UE position estimation most, while boosting the UE velocity and orientation estimation less.

2) *Euclidean Space vs. Riemannian Manifold*: Next, we examine the effectiveness of the proposed Riemannian manifold-based framework in enhancing tracking performance bench-

marked against conventional Euclidean techniques. Fig. 9 compares the estimation errors of the classical UKF in Euclidean space and the proposed UKF on Riemannian manifold. In this simulation, both methods utilize the proposed belief assignment (60). From Fig. 9, insights are obtained as follows:

- In general, without the presence of RISs, the tracking performance of the system exhibits superior performance in rural regions, deteriorates in suburban areas, and experiences the poorest performance in urban environments. This phenomenon arises due to the decreased Rician factor and channel gain in closer proximity to the urban environment, thereby diminishing overall system performance. However, upon the integration of RIS, similar to the results in Fig. 8, significant improvements are observed in the estimation of the UE position and velocity (particularly position) under both methodologies. This again confirms that the involvement of RISs can potentially mitigate the negative impact of urban attenuation. Conversely, the introduction of RISs contributes minimally to the estimation of the UE orientation.
- By comparing the UKF in Euclidean space and on Riemannian manifold, we observe that the two methods showcase a similar level of accuracy in the urban region with strong signal reception. Nonetheless, when it comes to the suburban and urban environments with weaker signal reception, the proposed Riemannian manifold-based UKF can consistently outperform the classical Euclidean UKF. Such superiority is particularly significant in the orientation estimation, verifying that the proposed UKF on the Riemannian manifold can effectively preserve the $SO(3)$ constraint and thus enhance the orientation estimation performance, which in turn benefits the position and velocity estimation as well.

C. The Impact of the State and Observation Uncertainty

Now we investigate how the state and observation uncertainty affect the tracking performance. As clarified in Section III-B, the uncertainty in the state arises from measurement errors in UE's acceleration and rotation, which can be represented by the standard deviation σ_a and σ_ω . On the other hand, the uncertainty on the observation is introduced by the estimation errors of the channel parameters, which can be controlled by the number of subcarriers K [10]. Typically, a greater number of subcarriers results in a higher FIM, thereby reducing the observation uncertainty in channel parameters. For compactness, here we only show the estimation performance of UE position and orientation while omitting the evaluation of UE velocity, due to the perturbation in the UE velocity is injected in the same pattern as that in the UE position, as demonstrated in (29). The behavior of the UE velocity is the same as the position.

1) *The Impact of σ_a :* We first evaluate the estimation root mean squared errors (RMSEs) of the UE position and orientation vs. the standard deviation σ_a of the UE acceleration measurement. In this evaluation, we compute the RMSE using the proposed Riemannian manifold-based UKF over $\sigma_a = \{0.1, 0.3, 0.5, 0.7\}$ m/s² for the cases: (i) $K = 300$;

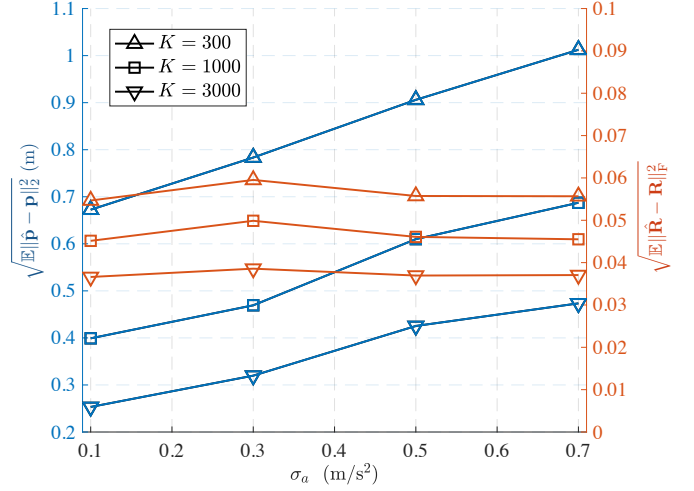


Fig. 10. The evaluation of the estimation errors in the UE position and orientation vs. the standard deviation σ_a of the UE acceleration measurement. The tests are conducted in different cases that $K = \{300, 1000, 3000\}$.

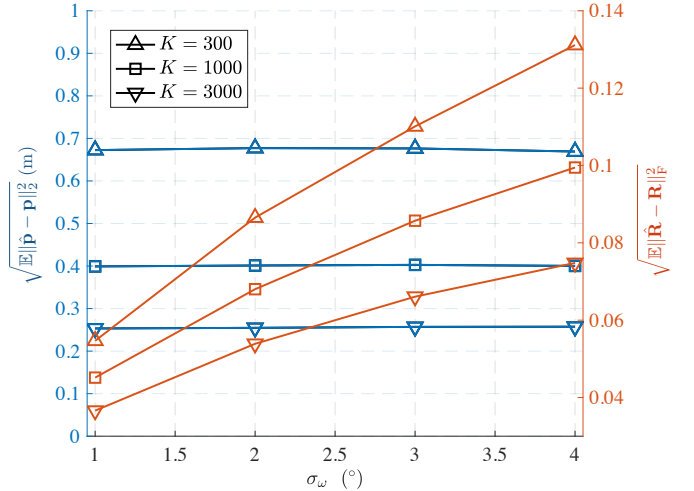


Fig. 11. The evaluation of the estimation errors in the UE position and orientation vs. the standard deviation σ_ω of the UE rotation measurement. The tests are conducted in different cases that $K = \{300, 1000, 3000\}$.

(ii) $K = 1000$; (iii) $K = 3000$. During this simulation, the standard deviation of the rotation measurement is fixed as $\sigma_\omega = 1^\circ$. The results are presented in Fig. 10. It is observed that the estimation RMSE of the UE position increases with an increase in σ_a , while that of the UE orientation keeps flat over different σ_a values. This phenomenon showcases the robustness of the proposed method in the orientation estimation to the acceleration measurement errors. Apart from that, it is observed that increasing the number of subcarriers K (i.e., reducing the uncertainty in the observation) can also effectively improve the estimation accuracy.

2) *The Impact of σ_ω :* Then we evaluate the estimation RMSEs of the UE position and orientation vs. the standard deviation $\sigma_\omega = \{1^\circ, 2^\circ, 3^\circ, 4^\circ\}$ of the UE rotation measurement. The simulation is carried out in the same setup as in Fig. 10 while the acceleration perturbation is fixed as $\sigma_a = 0.1$ m/s². The result is depicted in Fig. 11. Opposite

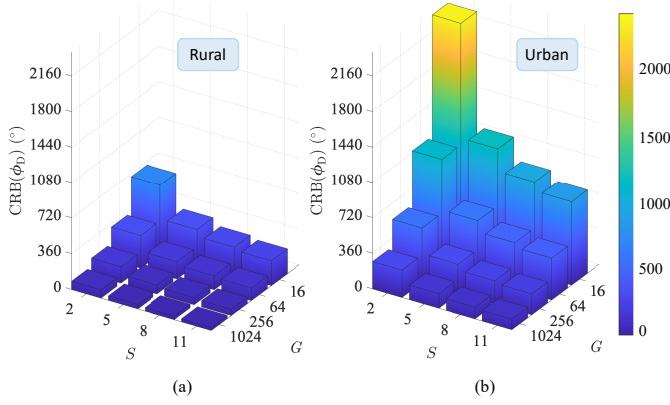


Fig. 12. The observation uncertainty vs. the transmission overhead. The observation uncertainty is represented by the CRB of ϕ_D while the transmission overhead is determined by the number of transmissions G and the number of satellites S . The evaluation is conducted under the rural and urban scenarios, respectively.

to the results in Fig. 10, we can observe from Fig. 11 that the estimation RMSE of the UE orientation increases with the increase of σ_ω , while the estimation RMSE of the UE position keeps flat over different σ_ω values. This indicates the robustness of the proposed method in the position estimation to the rotation measurement errors. In addition, the same phenomenon is observed that enlarging K can help improve tracking performance.

3) Observation Uncertainty vs. Transmission Overhead:

The results shown above indicate that reducing the uncertainty in the observations (by increasing K) can consistently improve the estimation performance for all unknowns. Besides the number of subcarriers K , the uncertainty in the observations can also be lowered by increasing the number of transmissions G and the number of satellites S . However, increasing G or S can also notably increase the transmission overhead. As demonstrated in Fig. 3, the total overhead during a single update interval T_U is GS . Therefore, we now evaluate the observation uncertainty vs. transmission overhead. Specifically, we select a time instant n in the RIS-visible area and compute the CRB of the AoDs ϕ_D from the RISs to the UE as a representative of the uncertainty in the observation, which is given by

$$\text{CRB}(\phi_D) = \sqrt{\text{Tr}([\mathbf{J}^{-1}(\zeta_n)]_{R+1:3R, R+1:3R})}. \quad (68)$$

Fig. 12 presents the evaluation of $\text{CRB}(\phi_D)$ vs. $\{G, S\}$, where both the rural and urban scenarios are assigned and tested. It is clearly shown that there exists a trade-off between the transmission overhead and the observation uncertainty. Generally, increasing the number of transmissions or satellites can always help reduce the uncertainty in the channel parameter observations. Comparing the results in the rural and urban environments, we can further conclude that the urban environment would also increase the uncertainty in the channel parameters due to the higher signal attenuation. Hence, it is suggested that a higher transmission overhead is required in urban regions to combat this uncertainty elevation.

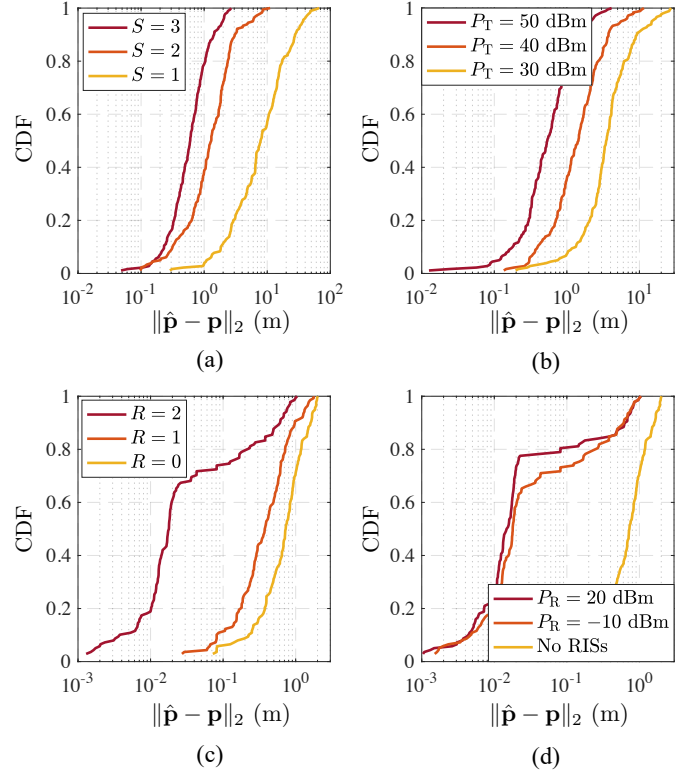


Fig. 13. The CDF evaluation of the estimation RMSEs of the UE position under different system setups. (a) The number of satellites $S = \{1, 2, 3\}$. (b) The satellite transmission power $P_T = \{30 \text{ dBm}, 40 \text{ dBm}, 50 \text{ dBm}\}$. (c) The number of RISs $R = \{0, 1, 2\}$. (d) The power supply of RISs $P_R = \{-10 \text{ dBm}, 20 \text{ dBm}\}$ and the case without RISs.

D. The Impact of the System Configuration

Finally, Fig. 13 illustrates the cumulative distribution function (CDF) of the estimation error of the UE position over different system setups. These results demonstrate the impact of the system parameters including the number of LEO satellites S , the transmission power at LEO satellites P_T , the number of RISs R , and the power supply of RISs P_R . To better illustrate the impact of these parameters, the CDFs over different RIS numbers and powers (i.e., Fig. 13-(c) and Fig. 13-(d)) are collected from the RISs-visible urban region only. It is observed that increasing the number of satellites or the transmission power of satellites can effectively enhance the overall tracking performance. On the other hand, by adding more RISs or elevating the RIS power supply, the tracking performance can also be improved. This indicates that both LEO satellites and RISs contribute to improving tracking performance and the collaboration between them showcases a promising potential for advanced user tracking solutions across complex environments.

VI. CONCLUSION

This paper studies the 9D user tracking problem within a hybrid terrestrial and non-terrestrial wireless system, integrating LEO satellites and RISs. A novel Riemannian manifold-based UKF method is proposed to simultaneously track the 3D position, 3D velocity, and 3D orientation of a ground user,

effectively handling challenges posed by nonlinear observation functions, constrained UE states, and unknown observation statistics. Numerical simulations demonstrate the effectiveness and robustness of the proposed tracking method. Meanwhile, it is also revealed that the inclusion of RISs can substantially enhance the tracking performance. Given the potential of such hybrid networks, future research could focus on optimizing collaborative beamforming design, developing effective protocols, and exploring the multipath effect.

APPENDIX A CALCULATION OF FIM \mathbf{J}

In addition to $\boldsymbol{\rho}$ defined in (21), for each satellite, we can further collect the other unknown nuisance parameters as

$$\boldsymbol{\xi}_s = [\Re(\alpha_s^0), \Im(\alpha_s^0), \Re(\alpha_r^0), \Im(\alpha_r^0)]^T \in \mathbb{R}^{2(R+1)}, \quad (1)$$

where $\alpha_r^0 \in \mathbb{C}^R$ is a vector collecting α_r^0 , $r = 1, 2, \dots, R$. Furthermore, we stack the noise-free version of received signals from the s -th satellite over G transmissions and K subcarriers as

$$\boldsymbol{\ell}_s = [\ell_s^1(1), \dots, \ell_s^K(1), \dots, \ell_s^1(g), \dots, \ell_s^K(g), \dots, \ell_s^1(G), \dots, \ell_s^K(G)]^T \in \mathbb{C}^{GK}. \quad (2)$$

By assuming the noise at the signal across different transmissions, subcarriers, and satellites are independent, we can define the following covariance matrix of the received signals

$$\mathbf{C} = \text{blkdiag}(\mathbf{C}_1, \dots, \mathbf{C}_s, \dots, \mathbf{C}_S), \quad (3)$$

where $\mathbf{C}_s = \text{diag}([C_s^1(1), \dots, C_s^K(1), \dots, C_s^1(g), \dots, C_s^K(g), \dots, C_s^1(G), \dots, C_s^K(G)]^T)$. Then, according to the Slepian-Bangs formula [38], the FIM of the channel parameters can be calculated as

$$\mathbf{J}_{\text{ch}} = 2\Re(\mathbf{D}^H \mathbf{C}^{-1} \mathbf{D}), \quad (4)$$

where the Jacobian matrix \mathbf{D} is defined as

$$\mathbf{D} = \begin{bmatrix} \frac{\partial \ell_1}{\partial \boldsymbol{\rho}_0} & \frac{\partial \ell_1}{\partial \boldsymbol{\rho}_1} & \dots & \mathbf{0} & \frac{\partial \ell_1}{\partial \boldsymbol{\xi}_1} & \dots & \mathbf{0} \\ \vdots & \vdots & \ddots & \vdots & \vdots & \ddots & \vdots \\ \frac{\partial \ell_S}{\partial \boldsymbol{\rho}_0} & \mathbf{0} & \dots & \frac{\partial \ell_S}{\partial \boldsymbol{\rho}_S} & \mathbf{0} & \dots & \frac{\partial \ell_S}{\partial \boldsymbol{\xi}_S} \end{bmatrix}. \quad (5)$$

Since we do not extract any information from nuisance parameters vectors $\boldsymbol{\xi}_s$, $s = 1, \dots, S$, the corresponding contribution of these parameters to FIM \mathbf{J}_{ch} needs to be removed. To this end, we partition \mathbf{J}_{ch} as

$$\mathbf{J}_{\text{ch}} = \begin{bmatrix} \mathbf{X} & \mathbf{Y} \\ \mathbf{Y}^T & \mathbf{Z} \end{bmatrix}, \quad (6)$$

where the dimension of \mathbf{X} is $(5R + (R+6)S) \times (5R + (R+6)S)$, and the dimension of \mathbf{Z} is $2S(R+1) \times 2S(R+1)$. Then the FIM of channel parameters without nuisance parameters can be calculated as

$$\mathbf{J} = \mathbf{X} - \mathbf{Y}\mathbf{Z}^{-1}\mathbf{Y}^T. \quad (7)$$

REFERENCES

- [1] B. Hofmann-Wellenhof, H. Lichtenegger, and E. Wasle, *GNSS—global navigation satellite systems: GPS, GLONASS, Galileo, and more*. Springer Science & Business Media, 2007.
- [2] L. Yang, J. Cao, W. Zhu, and S. Tang, “Accurate and efficient object tracking based on passive RFID,” *IEEE Transactions on Mobile Computing*, vol. 14, no. 11, pp. 2188–2200, 2015.
- [3] A. Manzanilla, S. Reyes, M. Garcia, D. Mercado, and R. Lozano, “Autonomous navigation for unmanned underwater vehicles: Real-time experiments using computer vision,” *IEEE Robotics and Automation Letters*, vol. 4, no. 2, pp. 1351–1356, 2019.
- [4] M. S. Grewal, L. R. Weill, and A. P. Andrews, *Global positioning systems, inertial navigation, and integration*. John Wiley & Sons, 2007.
- [5] G. Isbitiren and O. B. Akan, “Three-dimensional underwater target tracking with acoustic sensor networks,” *IEEE Transactions on Vehicular Technology*, vol. 60, no. 8, pp. 3897–3906, 2011.
- [6] M. Hashimoto, K. Takahashi, and Y. Matsui, “Moving-object tracking with multi-laser range sensors for mobile robot navigation,” in *IEEE International Conference on Robotics and Biomimetics (ROBIO)*, 2007, pp. 399–404.
- [7] V. Bahl and V. Padmanabhan, “Enhancements to the RADAR user location and tracking system,” Tech. Rep. MSR-TR-2000-12, February 2000. [Online]. Available: <https://www.microsoft.com/en-us/research/publication/enhancements-to-the-radar-user-location-and-tracking-system/>
- [8] J. Talvitie, M. Säily, and M. Valkama, “Orientation and location tracking of XR devices: 5G carrier phase-based methods,” *IEEE Journal of Selected Topics in Signal Processing*, vol. 17, no. 5, pp. 919–934, 2023.
- [9] C. Laoudias, A. Moreira, S. Kim, S. Lee, L. Wiroola, and C. Fischione, “A survey of enabling technologies for network localization, tracking, and navigation,” *IEEE Communications Surveys & Tutorials*, vol. 20, no. 4, pp. 3607–3644, 2018.
- [10] H. Chen, H. Saeeddeen, T. Ballal, H. Wymeersch, M.-S. Alouini, and T. Y. Al-Naffouri, “A tutorial on Terahertz-band localization for 6G communication systems,” *IEEE Communications Surveys & Tutorials*, vol. 24, no. 3, pp. 1780–1815, 2022.
- [11] W. Jiang, B. Han, M. A. Habibi, and H. D. Schotten, “The road towards 6G: A comprehensive survey,” *IEEE Open Journal of the Communications Society*, vol. 2, pp. 334–366, 2021.
- [12] S. Dang, O. Amin, B. Shihada, and M.-S. Alouini, “What should 6G be?” *Nature Electronics*, vol. 3, no. 1, pp. 20–29, 2020.
- [13] H. Tataria, M. Shafi, A. F. Molisch, M. Dohler, H. Sjöland, and F. Tufvesson, “6G wireless systems: Vision, requirements, challenges, insights, and opportunities,” *Proceedings of the IEEE*, vol. 109, no. 7, pp. 1166–1199, 2021.
- [14] H. Guo, J. Li, J. Liu, N. Tian, and N. Kato, “A survey on space-air-ground-sea integrated network security in 6G,” *IEEE Communications Surveys & Tutorials*, vol. 24, no. 1, pp. 53–87, 2022.
- [15] S. Liu, Z. Gao, Y. Wu, D. W. Kwan Ng, X. Gao, K.-K. Wong, S. Chatzinotas, and B. Ottersten, “LEO satellite constellations for 5G and beyond: How will they reshape vertical domains?” *IEEE Communications Magazine*, vol. 59, no. 7, pp. 30–36, 2021.
- [16] X. Luo, H.-H. Chen, and Q. Guo, “LEO/VLEO satellite communications in 6G and beyond networks – technologies, applications and challenges,” *IEEE Network (early access)*, 2024.
- [17] Z. M. Kassas, N. Khairallah, and S. Kozhaya, “Ad astra: Simultaneous tracking and navigation with megaconstellation LEO satellites,” *IEEE Aerospace and Electronic Systems Magazine*, pp. 1–19, 2024.
- [18] Z. M. Kassas, S. Kozhaya, H. Kanj, J. Saroufim, S. W. Hayek, M. Neinavaie, N. Khairallah, and J. Khalife, “Navigation with multi-constellation LEO satellite signals of opportunity: Starlink, OneWeb, Orbcomm, and Iridium,” in *IEEE/ION Position, Location and Navigation Symposium (PLANS)*, 2023, pp. 338–343.
- [19] Y. Su, Y. Liu, Y. Zhou, J. Yuan, H. Cao, and J. Shi, “Broadband LEO satellite communications: Architectures and key technologies,” *IEEE Wireless Communications*, vol. 26, no. 2, pp. 55–61, 2019.
- [20] R. M. Ferre, E. S. Lohan, H. Kuusniemi, J. Praks, S. Kaasalainen, C. Pinell, and M. Elsanhoury, “Is LEO-based positioning with megaconstellations the answer for future equal access localization?” *IEEE Communications Magazine*, vol. 60, no. 6, pp. 40–46, 2022.
- [21] P. Zheng, X. Liu, T. Ballal, and T. Y. Al-Naffouri, “5G-aided RTK positioning in GNSS-deprived environments,” in *31th European Signal Processing Conference (EUSIPCO)*, 2023.
- [22] Y. Liu, X. Liu, X. Mu, T. Hou, J. Xu, M. Di Renzo, and N. Al-Dhahir, “Reconfigurable intelligent surfaces: Principles and opportunities,” *IEEE*

- Communications Surveys & Tutorials*, vol. 23, no. 3, pp. 1546–1577, 2021.
- [23] H. Wymeersch, J. He, B. Denis, A. Clemente, and M. Juntti, “Radio localization and mapping with reconfigurable intelligent surfaces: Challenges, opportunities, and research directions,” *IEEE Vehicular Technology Magazine*, vol. 15, no. 4, pp. 52–61, 2020.
 - [24] R. Wang, Y. Yang, B. Makki, and A. Shamim, “A wideband reconfigurable intelligent surface for 5G millimeter-wave applications,” *IEEE Transactions on Antennas and Propagation (early access)*, 2024.
 - [25] H. Chen, P. Zheng, M. F. Keskin, T. Al-Naffouri, and H. Wymeersch, “Multi-RIS-enabled 3D sidelink positioning,” *IEEE Transactions on Wireless Communications (early access)*, 2024.
 - [26] J. He, F. Jiang, K. Keykhosravi, J. Kokkonen, H. Wymeersch, and M. Juntti, “Beyond 5G RIS mmWave systems: Where communication and localization meet,” *IEEE Access*, vol. 10, pp. 68 075–68 084, 2022.
 - [27] P. Zheng, H. Chen, T. Ballal, H. Wymeersch, and T. Y. Al-Naffouri, “Misspecified cramer-rao bound of RIS-aided localization under geometry mismatch,” in *IEEE International Conference on Acoustics, Speech and Signal Processing (ICASSP)*, 2023.
 - [28] P. Zheng, H. Chen, T. Ballal, M. Valkama, H. Wymeersch, and T. Y. Al-Naffouri, “JrCUP: Joint RIS calibration and user positioning for 6G wireless systems,” *IEEE Transactions on Wireless Communications (early access)*, 2023.
 - [29] W. U. Khan, E. Lagunas, A. Mahmood, S. Chatzinotas, and B. Ottersten, “RIS-assisted energy-efficient LEO satellite communications with NOMA,” *IEEE Transactions on Green Communications and Networking (early access)*, 2023.
 - [30] K. Tekbryk, G. K. Kurt, and H. Yanikomeroglu, “Energy-efficient RIS-assisted satellites for IoT networks,” *IEEE Internet of Things Journal*, vol. 9, no. 16, pp. 14 891–14 899, 2022.
 - [31] P. Zheng, X. Liu, J. He, G. Seco-Granados, and T. Y. Al-Naffouri, “LEO satellite and RIS: Two keys to seamless indoor and outdoor localization,” *arXiv preprint arXiv:2312.16946*, 2023.
 - [32] B. L. Stevens, F. L. Lewis, and E. N. Johnson, *Aircraft control and simulation: dynamics, controls design, and autonomous systems*. John Wiley & Sons, 2015.
 - [33] C. Hertzberg, R. Wagner, U. Frese, and L. Schröder, “Integrating generic sensor fusion algorithms with sound state representations through encapsulation of manifolds,” *Information Fusion*, vol. 14, no. 1, pp. 57–77, 2013.
 - [34] M. Brossard, A. Barrau, and S. Bonnabel, “A code for unscented kalman filtering on manifolds (UKF-M),” in *IEEE International Conference on Robotics and Automation (ICRA)*, 2020, pp. 5701–5708.
 - [35] X. Liu, T. Ballal, H. Chen, and T. Y. Al-Naffouri, “Constrained wrapped least squares: A tool for high-accuracy GNSS attitude determination,” *IEEE Transactions on Instrumentation and Measurement*, vol. 71, pp. 1–15, 2022.
 - [36] J. He, H. Wymeersch, and M. Juntti, “Channel estimation for RIS-aided mmWave MIMO systems via atomic norm minimization,” *IEEE Transactions on Wireless Communications*, vol. 20, no. 9, pp. 5786–5797, 2021.
 - [37] J. Chen, Y.-C. Liang, H. V. Cheng, and W. Yu, “Channel estimation for reconfigurable intelligent surface aided multi-user mmWave MIMO systems,” *IEEE Transactions on Wireless Communications*, vol. 22, no. 10, pp. 6853–6869, 2023.
 - [38] S. M. Kay, *Fundamentals of statistical signal processing: estimation theory*. Prentice-Hall, Inc., 1993.
 - [39] P. Zheng, T. Ballal, H. Chen, H. Wymeersch, and T. Y. Al-Naffouri, “Coverage analysis of joint localization and communication in THz systems with 3D arrays,” *IEEE Transactions on Wireless Communications (early access)*, 2023.
 - [40] A. Abdi, W. Lau, M.-S. Alouini, and M. Kaveh, “A new simple model for land mobile satellite channels: first- and second-order statistics,” *IEEE Transactions on Wireless Communications*, vol. 2, no. 3, pp. 519–528, 2003.
 - [41] D.-H. Jung, J.-G. Ryu, W.-J. Byun, and J. Choi, “Performance analysis of satellite communication system under the shadowed-Rician fading: A stochastic geometry approach,” *IEEE Transactions on Communications*, vol. 70, no. 4, pp. 2707–2721, 2022.
 - [42] E. Kim, I. P. Roberts, and J. G. Andrews, “Downlink analysis and evaluation of multi-beam LEO satellite communication in shadowed Rician channels,” *IEEE Transactions on Vehicular Technology*, pp. 1–16, 2023.
 - [43] A. Goldsmith, *Wireless communications*. Cambridge university press, 2005.
 - [44] E. Wan and R. Van Der Merwe, “The unscented Kalman filter for nonlinear estimation,” in *Proceedings of the IEEE Adaptive Systems for Signal Processing, Communications, and Control Symposium (Cat. No.00EX373)*, 2000, pp. 153–158.
 - [45] A. H. Sayed, *Inference and Learning from Data: Inference*. Cambridge University Press, 2022, vol. 2.
 - [46] J. M. Lee, *Introduction to Riemannian manifolds*. Springer, 2018, vol. 2.
 - [47] N. Boumal, *An introduction to optimization on smooth manifolds*. Cambridge University Press, 2023.
 - [48] D. Koks, *Explorations in mathematical physics: the concepts behind an elegant language*. Springer, 2006.
 - [49] J. Lawson and Y. Lim, “Karcher means and karcher equations of positive definite operators,” *Transactions of the American Mathematical Society, Series B*, vol. 1, no. 1, pp. 1–22, 2014.
 - [50] F. Burkhardt, S. Jaeckel, E. Eberlein, and R. Prieto-Cerdeira, “QuADriGa: A MIMO channel model for land mobile satellite,” in *proc. of the 8th European Conference on Antennas and Propagation (EuCAP)*, 2014, pp. 1274–1278.
 - [51] S. Zhu, T. S. Ghazaany, S. M. R. Jones, R. A. Abd-Alhameed, J. M. Noras, T. Van Buren, J. Wilson, T. Suggett, and S. Marker, “Probability distribution of Rician k -factor in urban, suburban and rural areas using real-world captured data,” *IEEE Transactions on Antennas and Propagation*, vol. 62, no. 7, pp. 3835–3839, 2014.
 - [52] 3GPP TR 38.811 v15.4.0, “Study on new radio (NR) to support non-terrestrial networks (release 15),” *Tech. Rep.*, Sept. 2020.
 - [53] S. Jaeckel, L. Raschkowski, and L. Thiele, “A 5G-NR satellite extension for the QuaDRiGa channel model,” in *Joint European Conference on Networks and Communications & 6G Summit (EuCNC/6G Summit)*, 2022, pp. 142–147.
 - [54] International Telecommunication Union (ITU), “Attenuation by atmospheric gases and related effects,” P Series, Radiowave propagation, document ITU-R P.676-12, 2019.
 - [55] A. Hourani, “Atmospheric absorption loss for satellite communications,” *MATLAB Central File Exchange*, Retrieved Feb. 28, 2024. [Online]. Available: <https://www.mathworks.com/matlabcentral/fileexchange/78865-atmospheric-absorption-loss-for-satellite-communications>